

The cored distribution of dark matter in spiral galaxies

G. Gentile^{1*}, P. Salucci², U. Klein¹, D. Vergani^{1,3} and P. Kalberla¹

¹ *Radioastronomisches Institut der Universität Bonn, Auf dem Hügel 71, 53121 Bonn, Germany*

² *SISSA, via Beirut 4, 34014 Trieste, Italy*

³ *Observatoire de Paris, GEPI, CNRS UMR 8111 and Université Paris 7, 5 place Jules Janssen, 92195 Meudon Cedex, France*

Accepted Received

ABSTRACT

We present the HI data for 5 spiral galaxies that, along with their H α rotation curves, are used to derive the distribution of dark matter within these objects. A new method for extracting rotation curves from HI data cubes is presented; this takes into account the existence of a warp and minimises projection effects. The rotation curves obtained are tested by taking them as input to construct model data cubes that are compared to the observed ones: the agreement is excellent. On the contrary, the model data cubes built using rotation curves obtained with standard methods, such as the first-moment analysis, fail the test. The HI rotation curves agree well with the H α data, where they coexist. Moreover, the combined H α + HI rotation curves are smooth, symmetric and extended to large radii.

The rotation curves are decomposed into stellar, gaseous and dark matter contributions and the inferred density distribution is compared to various mass distributions: dark haloes with a central density core, Λ Cold Dark Matter (Λ CDM) haloes (NFW, Moore profiles), HI scaling and MOND. The observations point to haloes with constant density cores of size $r_{core} \sim r_{opt}$ and central densities scaling approximately as $\rho_0 \propto r_{core}^{-2/3}$. Λ CDM models (which predict a central cusp in the density profile) are in clear conflict with the data. HI scaling and MOND cannot account for the observed kinematics: we find some counter-examples.

Key words: galaxies: methods: data analysis – kinematics and dynamics – galaxies: spiral – dark matter.

1 INTRODUCTION

One of the tantalising and yet unanswered questions of contemporary astrophysics is that concerning the nature of dark matter (DM). While its existence has been inferred for several decades, only in the recent past its amount has been carefully assessed on various astrophysical scales. On galaxy scales, the classical and still most powerful tool to unveil DM is that of rotation curves. Compared to the pioneering work of Rubin, Thonnard & Ford (1980) and Bosma (1981), modern studies take advantage from greatly improved observational techniques, facilitating much more significant validations of cosmological theories, such as Cold Dark Matter (CDM). Although the prime astrophysical importance of the juxtaposition of observations and models was assessing the amount of DM in galaxies (Persic & Salucci 1988), the timed question has become its *distribution*. This issue directly pertains to the nature of this component, since a precise knowl-

edge of the density profile $\rho(R)$ is likely to be decisive: the DM nature is likely to determine the halo properties.

Yet, a wealth of observations have not been able to settle but the most fundamental issues, such as the validity of the CDM scenario on galactic scales (e.g. Navarro et al. 1996, Moore et al. 1998). Some of the shortcomings on the observational side were related to the limitations of optical rotation curves (internal rms, limited radial extent, dust contamination), while radio studies were affected by the well-known limited spatial resolution. Nevertheless, progress has been made, due to the increasing number of investigations on dwarf spirals and low-surface brightness (LSB) galaxies. These studies cast serious doubts on one of the fundamental properties of CDM haloes, namely their ‘cuspiness’ in the galaxy centres, and infer the presence of large core radii in the DM density profiles (see e.g. Flores & Primack 1994, Moore 1994, Burkert & Silk 1997, Kravtsov et al. 1998, McGaugh et al. 1998, Salucci & Burkert 2000, de Blok, McGaugh & Rubin 2001, Salucci 2001, de Blok & Bosma 2002, Salucci, Walter & Borriello 2003, Weldrake, de Blok & Walter 2003, Simon et al. 2003).

* E-mail: ggentile@astro.uni-bonn.de

However, due to the many steps in the data analysis, there can be subtle systematic errors that could distort the results or in any case render the results very poorly constrained. This has triggered off the recent debate concerning the reliability of the data and how well the mass models are really constrained. There are claims that the observations could actually be consistent with the dark matter density profiles predicted by the CDM simulations, not only by considering the HI data alone (van den Bosch et al. 2000 and van den Bosch & Swaters 2001), but also by combining H α and HI data (Primack 2002 and Swaters et al. 2003a). This is the reason why particular care should be taken in choosing a suited sample and in performing the data analysis. Note that recent simulations (e.g. Navarro et al. 2003) do not converge to a well-defined value of the inner slope down to the resolution limit (about 1 kpc), even though the slope of the dark matter density profile (defined as $-d\ln\rho/d\ln r$) at 1% of the virial radius is still about 1.2 for a typical galaxy. Notice also that the observational results on spiral galaxies show a discrepancy with the standard Λ CDM predictions well beyond 1 kpc, i.e. well beyond the resolution limit of the simulations.

In this paper we study a *sample* of galaxy rotation curves ideal for deriving the properties of the dark matter haloes around galaxies; it consists of five late-type bulge-less normal (high surface brightness) spiral galaxies; compared to the sample of Borriello & Salucci (2001) we have the same resolution in the central regions, but a larger spatial extension allowing us to determine the size of the core radii. One of the main concerns is that the rotation curve has both a high spatial resolution and a large extension, i.e. beyond the optical radius; this is typically achieved by combining optical (H α) and radio (HI) data (see e.g. de Blok & Bosma 2002 and Swaters et al. 2003a). The former provide the necessary high resolution (1" . . . 2") while the latter allow us to trace the potential out to large radii, typically 2–3 times the optical radius. It has been known for a long time that HI data usually suffer from the lack of resolution, which can affect the results, especially in the innermost parts; this problem is nicely reviewed by van den Bosch et al. (2000).

The difficulty in deriving reliable rotation curves from HI data cubes resides in the fact that a data cube is 4-dimensional (RA, dec, flux density and radial velocity), while the rotation curve is 2-dimensional (rotation velocity vs. radius). This means that starting from the data cube we have to take into account two types of considerations: one concerning the *positions* in which the rotation curve should be traced, i.e. how to reduce the spatial dimensions from (RA, Dec) to galactocentric radius. This is usually achieved by taking the position-velocity diagram along the major axis or by fitting concentric ellipses around the centre (tilted-ring modelling of the velocity field). The other consideration concerns the *rotation velocities* that should be attributed to these galactocentric radii: at the positions defined above we want to associate only one of the possible velocities that could in principle be derived from the spectra at single points (flux density vs. radial velocity), i.e. the radial component of the rotation velocity at that radius. This is usually done via different methods, most of them assuming symmetry of the profiles, like the first-moment analysis (the intensity weighted mean), or the single Gaussian fitting; therefore, when the profiles are not symmetric, i.e. in galax-

ies with a high inclination and/or a poor to intermediate resolution, these methods cannot be applied.

We have developed a new method for both of these considerations: a) concerning the positions, we traced the rotation curve along the ridge of the warp (this step is discussed in Vergani et al. 2004), when the velocity field was not sufficiently sampled (i.e., for the galaxies ESO 116-G12, ESO 287-G13, ESO 79-G14 and NGC 7339) and the tilted-ring modelling of the velocity field was therefore not possible; b) for the velocities we only considered the velocity side of the profiles opposite to the systemic velocity, and then corrected for the effects that artificially broaden the profile, i.e.: the turbulence of the ISM, the instrumental velocity resolution and the beam-broadening. The present paper concentrates on step b).

When both steps a) and b) were applied we called our method WAMET (WArped Modified Envelope Tracing method); when only step b) was applied and a velocity field was constructed (i.e., when the velocity field was sufficiently sampled, the case of NGC 1090) we called our method MET (Modified Envelope Tracing method). These approaches were tested by constructing artificial data cubes based on geometrical models of the HI disc that were iteratively compared to the observed data cubes. The MET/WAMET method proves to provide a better initial estimate of the rotation curve than more traditional methods, such as the first-moment analysis and the single-Gaussian fitting. Modelling the data cubes results in a powerful way to test and improve the derived rotation curves, as shown e.g. by Gentile et al. (2003).

This work is structured as follows: in Section 2 we present the sample and optical data that were used in this study, in Section 3 we describe the HI observations and the data reduction and Section 4 shows the data analysis; in Section 5 we present the results of data analysis, the new method for extracting the rotation curves is shown in Section 6 and the comparison between the observed and the modelled data cubes is presented in Section 7. In Section 8 we introduce the different mass models that were considered; the results of the mass decompositions are shown in Section 9 and in Section 10 we draw the conclusions concerning the derivation of the rotation curves and the dark matter haloes around the galaxies of our sample.

Throughout this paper we adopted a value for the Hubble parameter $H_0=75 \text{ km s}^{-1} \text{ Mpc}^{-1}$.

2 THE SAMPLE

2.1 The relevance of the present sample

The present sample is ideal for the study of dark matter within galaxies, not only for the characteristics of the galaxies, but also for the quality of the data. Table 1 presents the galaxy sample and its physical characteristics. This sample allows us to investigate a range of luminosities approximately 1.5 mag fainter than L_* , ideal for investigating the dark matter component, because it starts dominating the kinematics at relatively small radii.

In Table 2, the crucial characteristics of the kinematical data are shown: optical data allow us to sample very well the region inside the characteristic radii of various dark matter

Table 1. Physical parameters of the galaxies. M_I is the I-band absolute magnitude and M_{HI} is the total HI mass, r_{HI} is the HI radius (defined as the radius at which the surface density drops below $1 M_{\odot} \text{pc}^{-2}$) and r_d is the exponential scale length. r_f is the farthest radius with data and r_{opt} is the optical radius (defined as $3.2r_d$) and RR us the radio resolution scale. The dynamical mass M_{dyn} is determined at r_f .

Galaxy name	ESO 116-G12	ESO 287-G13	ESO 79-G14	NGC 1090	NGC 7339
M_I (mag)	-20.0	-21.7	-21.4	-21.8	-20.6
M_{HI} (M_{\odot})	1.5×10^9	1.1×10^{10}	3.5×10^9	8.5×10^9	5.5×10^8
Inclination ($^{\circ}$)	74	78	84	64	79
r_{HI}/r_d	6.7	7.4	4.8	8.8	4.1
r_f (kpc)	11.4	24.9	17.7	29.7	5.4
r_{opt} (kpc)	5.4	10.5	12.4	10.9	4.9
r_f/RR	5.4	5.8	5.0	10.6	4.6
M_{dyn} (M_{\odot})	3.3×10^{10}	1.9×10^{11}	1.3×10^{11}	1.8×10^{11}	3.1×10^{10}

Table 2. Optical and radio resolution scales (indicated respectively as OR and RR), and r_f , in units of the scale radii of the Burkert and NFW density profiles.

Galaxy	OR/ r_{core}	RR/ r_{core}	OR/ r_s	RR/ r_s	r_f/r_{core}	r_f/r_s
ESO 116-G12	0.03	0.49	0.02	0.29	2.7	1.6
ESO 287-G13	0.01	0.18	0.02	0.29	1.0	1.7
ESO 79-G14	0.04	0.43	0.02	0.24	2.1	1.2
NGC 1090	0.04	0.32	0.03	0.23	3.4	2.5
NGC 7339	0.02	0.15	0.01	0.08	0.6	0.3

distributions, while HI data allow us to probe a region *larger* than these radii, which permits us to investigate the core radius phenomenon at large distances and consequently to constrain the size of the core radii (note, however, the case of NGC 7339 discussed in Appendix A).

The rotation curves used here consist of the $\text{H}\alpha$ data for the inner parts and the HI data for the outer parts. The claim of unreliability of observed kinematics put forward by Rhee, Klypin & Valenzuela (2003) does not apply here: a) the derivation of the HI rotation curve was performed in a more thorough and reliable way than the standard tilted-ring analysis on the velocity field; b) the galaxies studied here were at an inclination optimal to minimise projection effects; c) in the regions where they coexist, the $\text{H}\alpha$ and HI data (emerging from different physical processes) do agree, implying a high quality of the data¹. The small internal scatter inside the each radial bin indicates that, for the galaxies of our sample, the effects of non-circular motions are negligible (even though a more thorough investigation should involve 2-dimensional $\text{H}\alpha$ data), differently from the case shown by Swaters et al. (2003b). Moreover, it can be shown (see e.g. de Blok, McGaugh & Bosma 2003) that the bias towards lower velocity gradients in the rotation curve due to a misalignment between the slit with the kinematical axis is likely to be small.

¹ Note, however, that this is not entirely true for NGC 1090, in which for some radii the $\text{H}\alpha$ lie $\sim 10 \text{ km s}^{-1}$ above the HI data.

2.2 Optical data

The five galaxies of this sample were chosen from the sample of 967 galaxies with optical rotation curves presented by Persic & Salucci (1995), according to the following criteria: a) they belong to the “excellent” subsample (i.e. the two sides are symmetric, the data are extended out to at least r_{opt} and the number of data points is ≥ 30); b) they have a reasonably high total HI flux; c) they have a relatively low I-band luminosity ($M_I > -21.8$), d) they have a large angular size, and e) they have an inclination i suitable for HI studies ($50^{\circ} < i < 85^{\circ}$). For each galaxy, the raw $\text{H}\alpha$ data were binned in groups of 4 to 6 (Persic & Salucci 1995), and the given error is the uncertainty on the average value inside the radial bin. We took a “minimum error” equal to half the average error in order to avoid data points with unrealistically low errors that could bias the rotation curves decompositions; for the same reason, when a data point was clearly inconsistent with the two neighbouring points and the general trend of the rotation curve, the value of its error was increased. The complete description of the optical observations (spectroscopic and photometric) can be found in Mathewson, Ford & Buchhorn (1992) and Persic & Salucci (1995).

3 HI OBSERVATIONS AND REDUCTION

We observed ESO 116-G12, ESO 287-G13 and ESO 79-G14 with the Australia Telescope Compact Array in the 750 m and 1.5 km configurations; the resulting baselines range from 31 m to 1500 m. The galaxies were observed for 12 hrs in each configuration. The correlator setup yielded 512 channels of

Table 3. HI Observational parameters

Galaxy name	ESO 116-G12	ESO 287-G13	ESO 79-G14	NGC 1090	NGC 7339
RA	3 ^h 13 ^m 03 ^s .9	21 ^h 23 ^m 13 ^s .7	1 ^h 02 ^m 51 ^s .2	2 ^h 46 ^m 33 ^s .9	22 ^h 37 ^m 46 ^s .9
Dec	−57°23′27″	−45°46′20″	−65°36′36″	−0°14′50″	23°47′12″
Number of channels	256	256	256	2 × 64	2 × 64
Channel separation (kHz)	31.2	31.2	31.2	24.4	24.4
Synth. beam (arcsec)	30.4 × 24.4	32.6 × 24.6	27.4 × 23.0	17.6 × 14.7	13.9 × 13.5
Synth. beam (kpc)	2.3 × 1.8	5.6 × 4.2	4.0 × 3.4	3.1 × 2.6	1.2 × 1.2
Noise (mJy beam ^{−1})	1.2	1.2	1.1	0.8	0.7

width 15.6 kHz, resulting in a total bandwidth of 8 MHz. The data were subsequently Hanning-smoothed to have a better signal-to-noise ratio. The final spectral resolution was 31.2 kHz, corresponding to a velocity resolution of 6.6 km s^{−1}.

NGC 1090 and NGC 7339 were observed with the Very Large Array in the C configuration, with baselines ranging from 35 m to 3400 m. The galaxies were observed for 8 hrs with a correlator mode which had 4 IFs, each IF pair having slightly different frequency centres; this was done in order to find a compromise between velocity resolution and bandwidth. We had 2 × 64 channels of width 24.4 kHz and a total bandwidth of 2.685 MHz; taking into account the overlapping channels, the total number of channels is 112. The resulting velocity resolution is ∼ 5.2 km s^{−1}.

The standard flagging and calibration of the $u-v$ data from the ATCA observations was performed within the software package MIRIAD (Sault et al. 1991), while the VLA data observations were flagged and calibrated with the Astronomical Image Processing Software (AIPS). The rest of the reduction was performed in MIRIAD.

Using a number of line-free channels (10 . . . 40) on each side of the line, the continuum contribution to the $u-v$ data was calculated performing a linear fit; this contribution was then subtracted from the data. Then, we produced a data cube with ROBUST parameters (Briggs 1995) ranging from 0 to 0.3, to reach an ideal compromise between high signal-to-noise ratio and small beam size; these values correspond to a weighting scheme of the $u-v$ data intermediate between uniform and natural weighting. The data were then CLEANed, first on a small region with emission and then on the whole map, with a total of 2500 iterations per channel map. The data were then restored with a Gaussian beam. Depending on the galaxies, we obtained beam sizes ranging from 13″ to 33″. The observational parameters are listed in Table 3.

4 DATA ANALYSIS

From the CLEANed cubes, new cubes with lower resolution were constructed (with a beam size about twice the original). This was done in order to distinguish genuine emission from spurious one; we considered as having reliable emission all the regions with an intensity $> 2 \times \sigma$ in the low-resolution cube; spurious noise was also removed. Moment-0 maps (total intensity maps) were derived based on the “masked” cubes. They are shown in Fig. 1, superimposed with optical DSS images. The first contour is the “pseudo

3- σ ” level defined in a way similar to Verheijen & Sancisi (2001): we define the noise at a certain position in the total intensity map as:

$$\sigma_N^h = \left(\frac{N}{2} - \frac{1}{8} \right)^{\frac{1}{2}} \frac{4}{\sqrt{6}} \sigma^h \quad (1)$$

where N is the number of channels that have been added at each position in the total intensity map and σ^h is the noise in the Hanning-smoothed channel maps. The “pseudo 3- σ ” level is obtained by averaging all the pixels with a signal-to-noise ratio between 2.75 and 3.25.

5 OBSERVATIONAL RESULTS

From Fig. 1 we note that the galaxies have a relatively high inclination and the HI emission has a large (up to ∼ 3 times) extent compared to the optical disc. The HI masses (M_{HI}) given in Table 1 were calculated from the total intensity maps after primary-beam correction using the following relation:

$$M_{\text{HI}} = 2.36 \times 10^5 D^2 \int SdV \quad (2)$$

where M_{HI} is in M_{\odot} , D is the distance of the galaxy in Mpc and $\int SdV$ is the total HI flux density in the total intensity map, measured in Jy km s^{−1}. The HI masses are in agreement with previous single-dish measurements to within 20%, implying that we are not losing much extended emission due to missing zero spacings.

The radial distribution of the neutral hydrogen surface density is computed by integrating the total intensity map over concentric ellipses for NGC 1090 and by means of the Lucy method (Warmels 1988) for the other galaxies. The results are shown in Fig. 2, where one can notice that the data reach the region where $M_{\text{HI}}(< r)/r$ starts to decrease.

Since the velocity field of NGC 1090 is sufficiently sampled, it could be subjected to tilted-ring modelling (Begeman 1989). In this case the MET method was applied (see the next Section) to construct the velocity field and then the first estimate of the rotation curve was derived by performing a tilted-ring fit to the velocity field. In the other cases the combination of high inclination and a large beam (compared to the size of the galaxy) requires the use of the WAMET method: we traced the rotation curve along the warp on points defined like in García-Ruiz et al. (2002) and implemented for studies of the kinematics by Vergani et al. (2004) on the total intensity map, we fit Gaussians to the

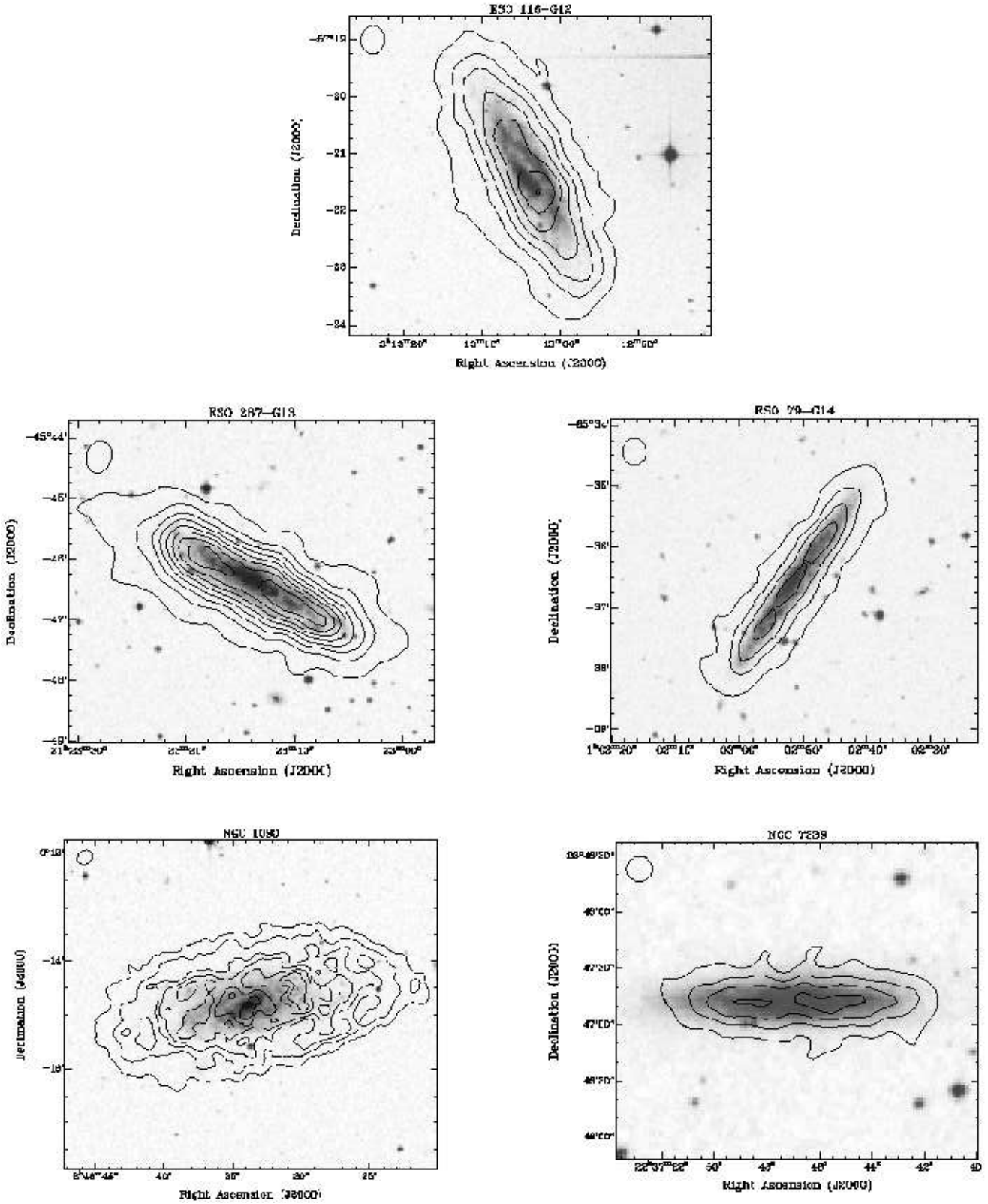


Figure 1. Optical DSS images (greyscale) superimposed with the HI total intensity map (contours). The first contour is the “pseudo $3\text{-}\sigma$ ” defined similarly to Verheijen & Sancisi (2001) and is equal to: $1.0 \times 10^{20} \text{atom cm}^{-2}$ for ESO 116-G12; $1.1 \times 10^{20} \text{atom cm}^{-2}$ for ESO 287-G13; $1.7 \times 10^{20} \text{atom cm}^{-2}$ for ESO 79-G14; $1.5 \times 10^{20} \text{atom cm}^{-2}$ for NGC 1090; $3.4 \times 10^{20} \text{atom cm}^{-2}$ for NGC 7339; the remaining contours are $(15, 30, 45, \dots) \times \sigma$, except for NGC 1090 and NGC 7339 where they are $(6, 12, 18, \dots) \times \sigma$. The beam is shown in the upper left corner.

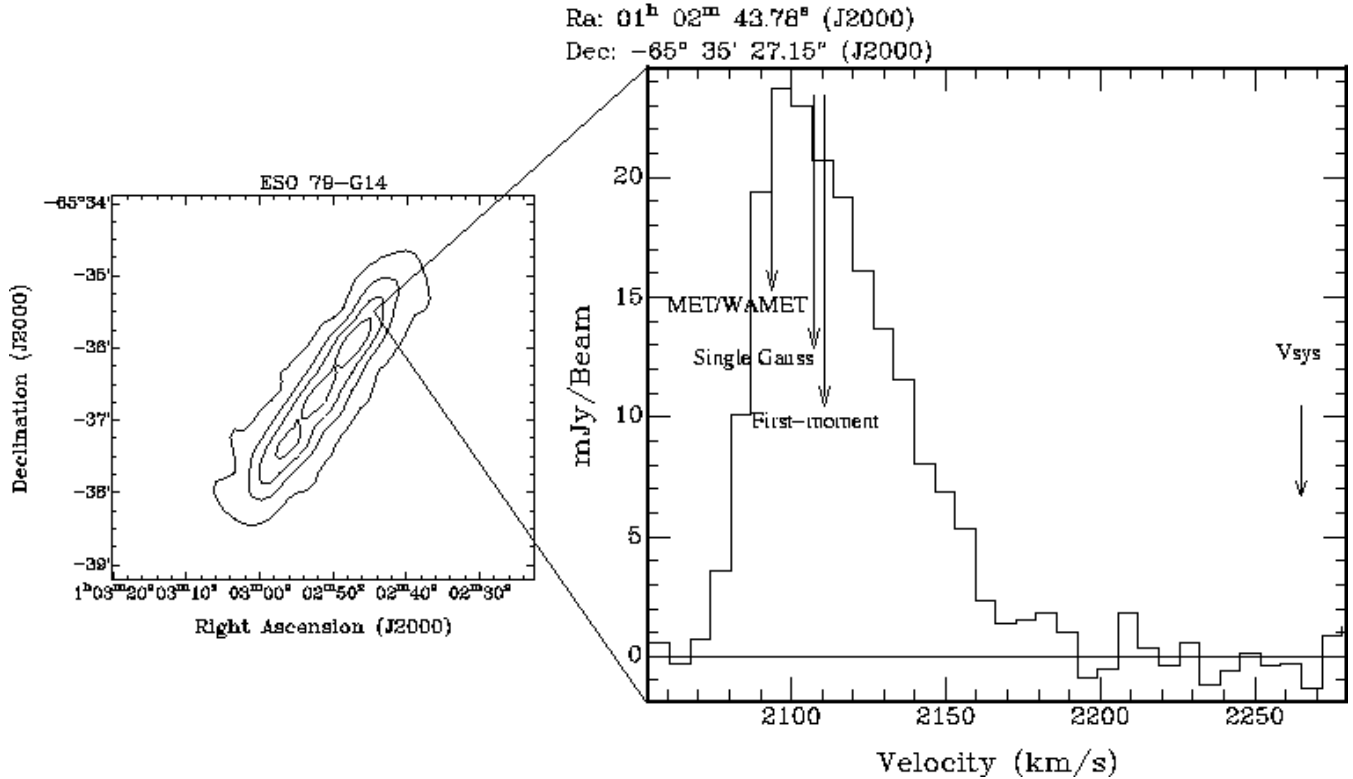


Figure 3. A typical spectrum of the galaxy ESO 79-G14 at an intermediate galactocentric distance. The arrows indicate the systemic velocity as well as the positions of the velocities derived from the MET/WAMET method, the first-moment analysis and by fitting a single Gaussian to the profiles.

density profiles parallel the minor axis, defining the position of the peak of the Gaussian as the “ridge” of the warp.

Concerning the analysis of the velocity profiles, particular care was taken in deriving the rotation velocity because they were in general asymmetric. In Fig. 3 we show an example of a typical profile at an intermediate galactocentric distance: it is not symmetric and it has a tail towards the systemic velocity. This is what we expect in case of a highly inclined galaxy, because (see Fig. 4) what we observe is the integration along a large portion of the disc, so that material with lower radial velocities also contributes to the velocity profile. Note, however, that Fig. 4 represents the extreme edge-on case: the galaxies studied here were chosen to have lower inclinations, so the portion of the disc intercepted by the line-of-sight is smaller.

Moreover, from recent results (Swaters, Sancisi & van der Hulst 1997, Fraternali et al. 2001), it seems that at least in some spiral galaxies there is evidence for neutral hydrogen at several kpc away from the galactic plane that rotates more slowly than the gas in the disc; this effect also produces an asymmetry of the velocity profiles in galaxies that do not have a high inclination. The result is that the standard methods (e.g. first-moment analysis and single-Gaussian fitting), which implicitly assume symmetry of the profiles, provide velocities that are biased towards the systemic velocity (see Fig. 3) and cannot be used to determine the true rotation velocity in the galaxies of our sample.

6 THE MODIFIED ENVELOPE-TRACING METHOD

In order to solve the problems discussed in the previous Section, we built a method similar to the Envelope-Tracing method (e.g. Sancisi & Allen 1979, Sofue et al. 1997); the aim is to fit only the side of the profiles which we are interested in, i.e. the extreme velocity side (with the assumption that the gas is present at these extreme velocities).

The first step was to fit a half-Gaussian from the peak of the profiles to their extreme velocity side (i.e. the side opposite to the systemic velocity), considering the velocity at half maximum, the terminal velocity (V_t). The rotation velocity V_{rot} at a certain position is then given by:

$$V_{rot} = \frac{|V_t - V_{sys}| - 0.5\sqrt{(\delta V_{ISM})^2 + (\delta V_{obs})^2 + (\delta V_b)^2}}{\sin i} \quad (3)$$

where i is the inclination, V_{sys} is the systemic velocity, and the terms indicated with δV describe the profile broadenings (in terms of full width to half maximum, FWHM):

δV_{ISM} is the broadening due to the turbulence of the interstellar medium, by assuming a constant velocity dispersion of the ISM, $\sigma_{ISM} = 10 \text{ km s}^{-1}$ (a typical value for spiral galaxies), which implies:

$$\delta V_{ISM} = \sigma_{ISM}\sqrt{8\ln 2} = 23.5 \text{ km s}^{-1}. \quad (4)$$

Notice that following Kamphuis (1993) (i.e. taking σ_{ISM} going from 12 to 7 km s^{-1}) would not significantly affect the derived rotation curves.

δV_{obs} is the instrumental contribution to the profile

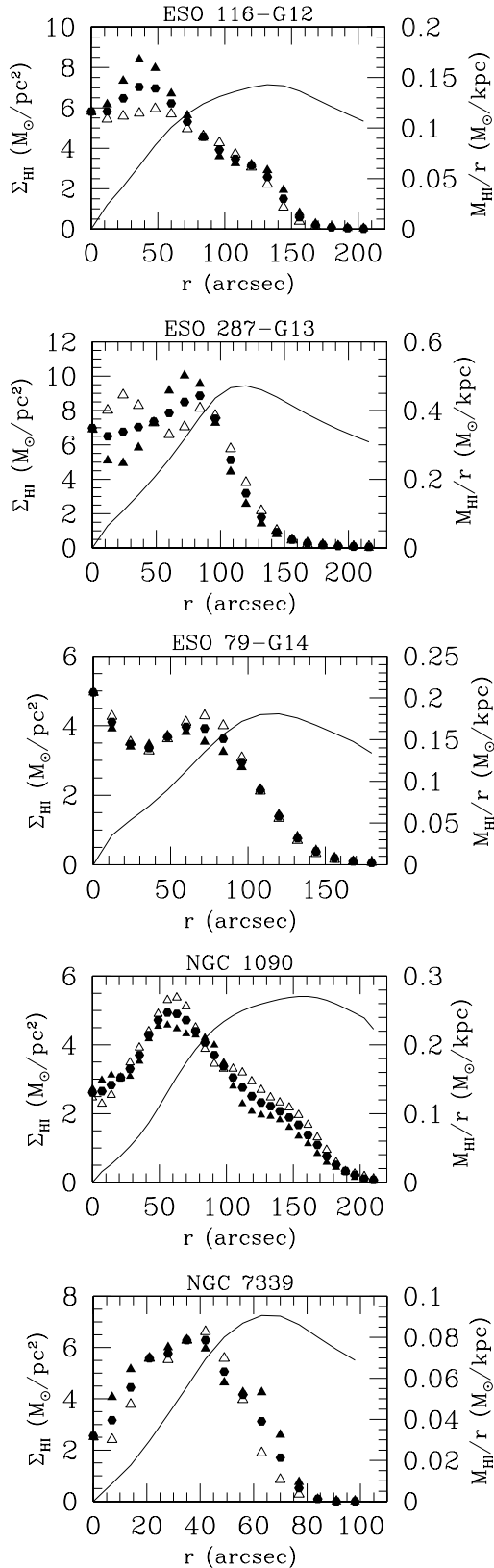


Figure 2. Radial distribution of the neutral hydrogen surface density (Σ_{HI}): the filled triangles denote the approaching side, the empty triangles the receding side and the filled circles the average. The solid line refers to the ratio $M_{\text{HI}}(<r)/r$, where $M_{\text{HI}}(<r)$ is the HI mass inside radius r .

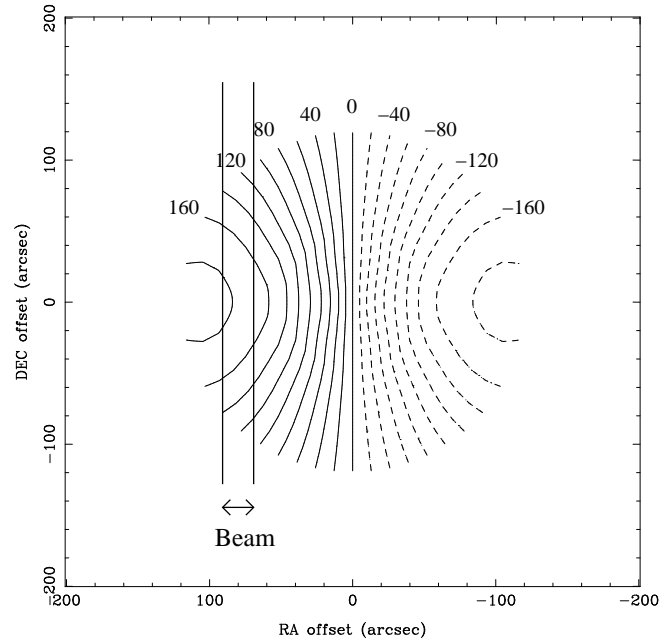


Figure 4. Model of the radial velocities in the plane of the galaxy ESO 79-G14 and the regions that would be intercepted by the beam in the edge-on case.

broadening, which we set equal to the channel resolution: 6.6 km s^{-1} for the galaxies observed with the ATCA and 5.2 km s^{-1} for those observed with the VLA.

δV_b is an estimate of the broadening of the profiles due to the beam: as is evident in Fig. 4, a larger beam will sample a larger portion of the velocity field and will thus broaden the profiles, even on their extreme velocity side. According to Sancisi & Allen (1979), a lower limit to δV_b can be given by setting it to zero, yielding an upper limit to the rotation velocity. To estimate an upper limit to δV_b , we assume as in Braun (1997), that the expected beam uncertainty in the profile widths is $2 \cdot [V(r \pm \theta_b/2) - V(r)]$, where the “+” corresponds to a positive gradient of the velocity field and “-” to a negative one; θ_b is the beam FWHM.

With an upper limit and a lower limit to δV_b , we decided to estimate δV_b using their average, i.e.:

$$\delta V_b = V(r \pm \theta_b/2) - V(r) \quad (5)$$

MET/WAMET has the following advantages:

- The profiles are asymmetric, thus methods assuming symmetry cannot be used to derive the rotation velocity; they would underestimate the rotation velocities, especially in the inner parts.
- We are only interested in the extreme velocity side of the profiles because it is not (or little) affected by projection effects.
- It also estimates the correction for the beam broadening of the profiles, which can be substantial in regions where the gradient of the velocity field is high.

The implemented method (WAMET) for warped galaxies can be applied to galaxies where the sampling of the velocity field is poor, and it enables us to trace the rotation curve along any possible warp instead of keeping a fixed position angle, like in methods based on the analysis of

the position-velocity diagram; the shortcomings of keeping a fixed position angle are discussed in Vergani et al. (2004).

7 ROTATION CURVES AND MODELS

In order to derive the rotation curves, we applied the tilted-ring modelling of the velocity field for NGC 1090. For the other galaxies we determined the kinematical centre and the systemic velocity by minimising the differences between the two sides. The errors are the maximum of the three following values: the difference between the velocities of the approaching and the receding sides, our correction for beam broadening of the profiles, and a “minimum error” equal to $(2/\sin i)$ km s⁻¹.

The MET/WAMET rotation curve served as an input to construct model data cubes with the task GALMOD within GIPSY (van der Hulst et al. 1992); these models have been then compared to the observed data cubes. Such models are built with the assumption that the neutral hydrogen moves along circular orbits; a series of geometrical and physical parameters, among which the rotation curve, allows us to create model observations of the HI discs. These models, when compared to the real data cubes, verify whether they are a fair representation of the HI disc. Some input parameters are inferred directly from the observations and kept fixed (e.g., the surface density profile), while others (e.g., the kinematical centre and the systemic velocity) are first estimated from the observations and then adjusted in order to optimise the match between the observed and the model cubes.

In two cases (ESO 287-G13 and NGC 1090, the galaxies with the steepest rotation curves) the rotation curve derived with MET/WAMET had to be slightly modified in order to better reproduce the observed data cubes. We found out that it was necessary to increase the value of the rotation velocity of the 2–3 innermost points by values of the order of their 1σ error; this is probably due to the fact that, even with the MET/WAMET method, when the rotation curve rises steeply we are not able to retrieve precisely the true rotation velocity; this is however possible by modelling the data cube. In Fig. 5, we display some channel maps (observed and modelled) to show that with our final rotation curves we are able to provide a very good reproduction of the observations. All the galaxies of our sample were successfully modelled with a small warp in the outer parts or with no warp at all. In particular, we found necessary to include in our model parameters a 5° clockwise warp in ESO 116-G12, a 2° clockwise warp in ESO 79-G14 and a 2° anti-clockwise warp in NGC 1090. Concerning the inclination as a function of radius, it was kept constant at the values given in Table 1, except for the galaxy ESO 79-G14, where a 5° decrease of the inclination in the outer parts was necessary to reproduce the shape of the extreme channels. The errors on the derived orientation angles are of a few degrees (Gentile et al. 2003).

Using the rotation curves derived from other methods provided data cubes that were clearly different from those observed. In Fig. 6, for the galaxy ESO 116-G12, we show some channel maps and the position-velocity diagram along the major axis of the observed data cube, of a model created from the corrected MET/WAMET rotation curve and of a model created from the first-moment rotation curve. The

latter clearly fails in reproducing some of the observed features, like the shape of the extreme channels and the slope of the position-velocity diagram. Fitting single Gaussians to the velocity profiles gives very similar results to the first-moment rotation curve.

In order to assess the validity of a model we used a number of tools to visualise the different properties of the data cube. In particular, the model has to simultaneously match the intensity and shape of the emission in the single channel maps, the column density distribution in the moment-0 map, and the intensity and shape of the emission in the position-velocity diagrams, along the major and minor axis and on slices displaced with respect to the galactic centre. The comparison of model data cubes to the observations is a very powerful and crucial test to check quality and reliability of the rotation curves.

In Fig. 7, we show the H α and HI rotation curves projected onto the HI position-velocity diagrams of the galaxies of our sample: the agreement between the two datasets is good and, as should be expected, the HI rotation curves follow the shape of the last contours of the position-velocity diagrams. The HI rotation curves agree with the H α data within 1σ for the bulk of the points. In the case of NGC 1090, however, at some radii there is an offset of about 10 km s⁻¹ between the two data sets: in Fig. 7 one can see that the H α data lie above the HI rotation curve; the figure shows that it is not an error in the HI data reduction, but rather an intrinsic difference, maybe due to non-circular motions associated with the small bar visible in the optical image. The optical image of ESO 116-G12 looks a bit asymmetric, but the kinematics is not, while the other galaxies look symmetric in both the kinematics and the photometry, which tells us that apart from NGC 1090 the effects of possible hidden bars are negligible. We plot about two points per beam for the HI rotation curve: this was done in order to have a comparable number of HI and H α points. Plotting fewer HI points would result in the H α data outnumbering the HI data and biasing the rotation curve fits.

We also compared the H α data with the HI rotation curves derived with two different methods (Fig. 8): our corrected MET/WAMET method and the first-moment. The latter yields a much worse agreement with the H α rotation curves, especially in the inner parts where the profiles are most asymmetric: in these cases the rotation velocities are severely underestimated. This shows the importance of the particular care that should be taken in deriving rotation curves.

The symmetry and smoothness of the rotation curves in the selected sample, along with the good agreement between the two datasets make these galaxies ideal laboratories for a dark matter study based on the kinematics: this holds in particular because they lack large non-circular motions, a major factor of disturbance and uncertainty in this kind of study. The agreement between the H α and HI rotation curves also tells us that any systematic errors that might artificially render the rotation curve shallower (i.e. extinction in the H α data, bad positioning of the slit, low resolution of the HI data) are small.

Note that the H α data are absolutely necessary for a mass decomposition such as the one presented in the next sections. The uncertainties in the inner parts of the HI rotation curves are quite large (typically 10–20 km s⁻¹), there-

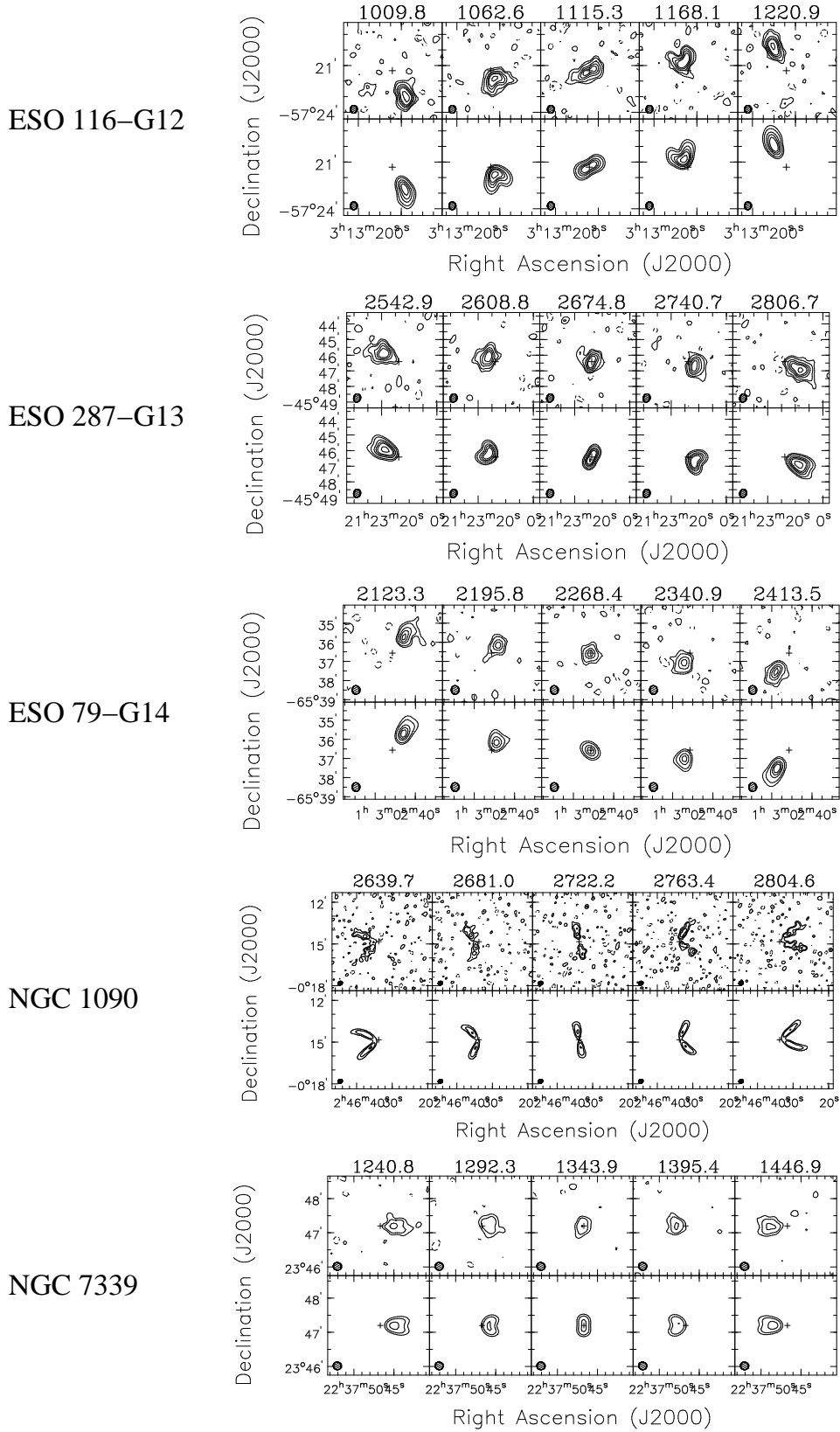


Figure 5. Five representative observed channel maps (upper panels) with the correspondent channel maps of the model data cubes (lower ones). The heliocentric radial velocities are indicated above each plot. The central map has a velocity closest to systemic. The cross indicates the centre of the galaxy. Contours are -4σ , -2σ , 2σ , 4σ , then 10, 15, 20, 30, 50 mJy beam⁻¹ for the ATCA galaxies, and -4σ , -2σ , 2σ , 4σ , then 6, 10, 15, 20, 30, 50 mJy beam⁻¹ for the VLA galaxies. The beam is shown in the lower left corner.

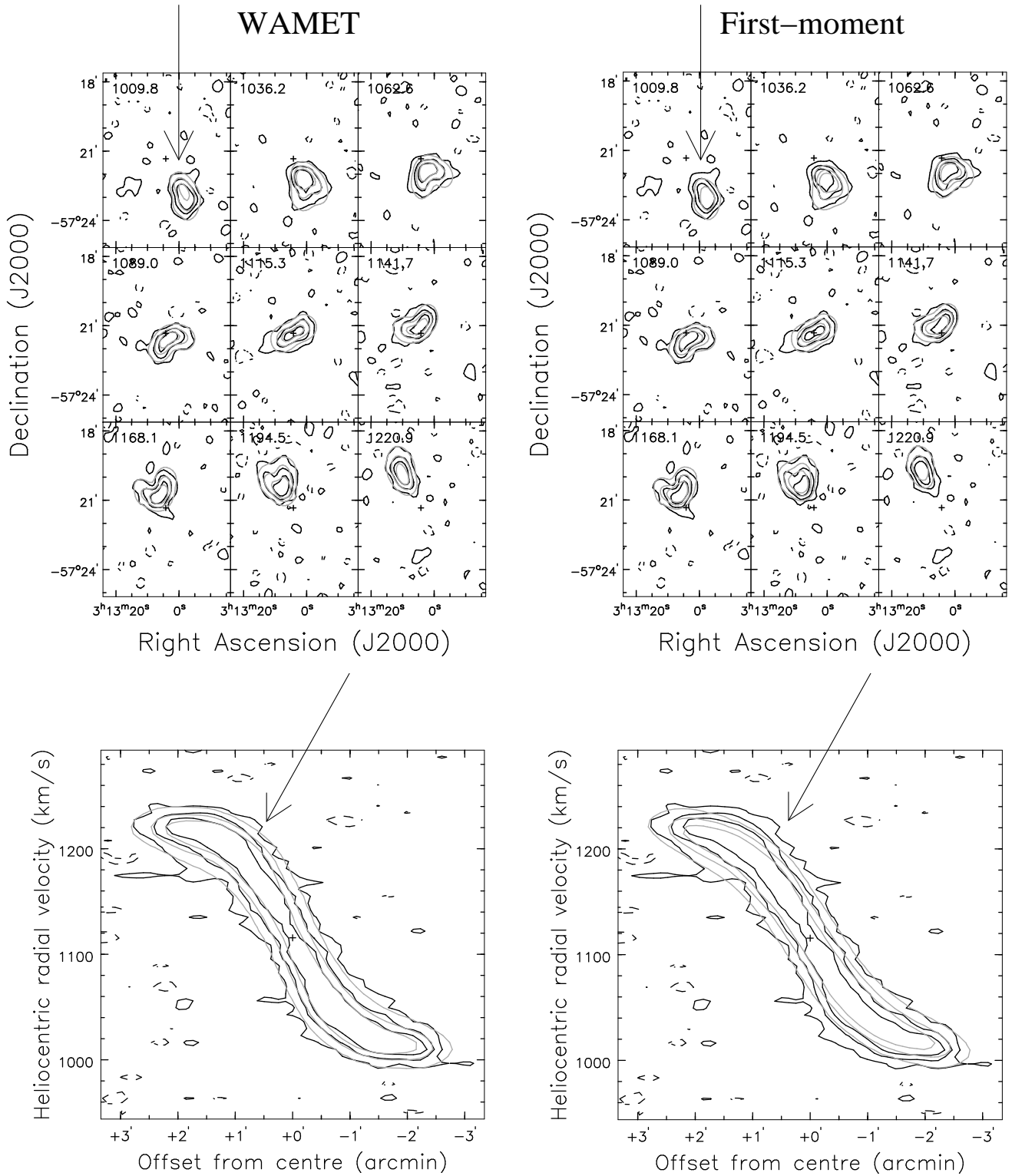


Figure 6. Comparison between the *observed* data cube and two *model* data cubes for ESO 116-G12: the MET/WAMET rotation curve (left) and the first-moment analysis rotation curve (right); the black contours trace the observed data cube and the grey contours trace the model data cubes. On the top we show some representative channel maps (the heliocentric radial velocities are shown in the upper left corners) and at the bottom the position-velocity diagrams along the major axis. The contours are $-2.5, 2.5, 10, 20, 50$ mJy beam $^{-1}$. The cross indicates the centre of the galaxy and the arrows show some key positions where the difference between the two model data cubes is noticeable.

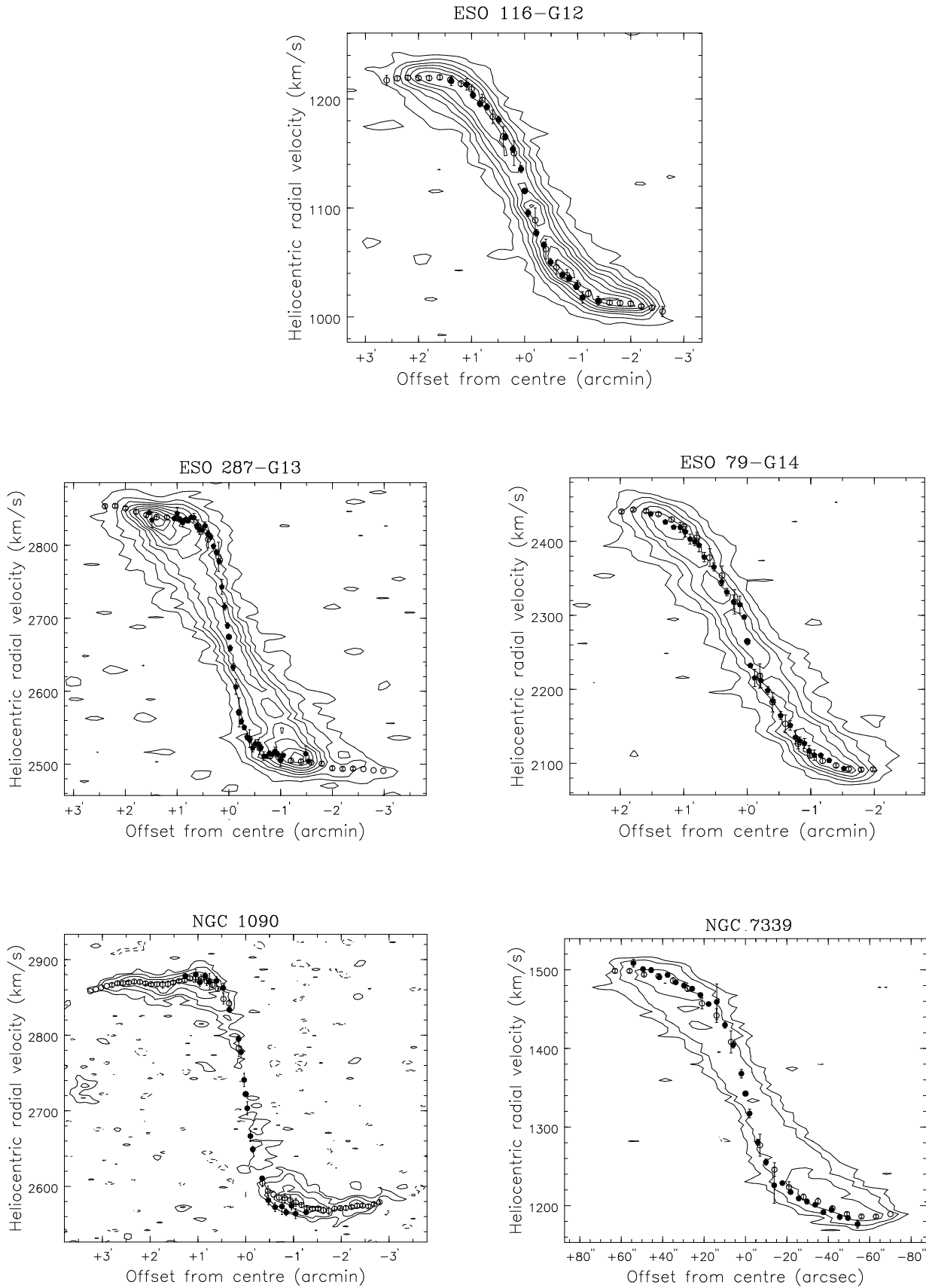


Figure 7. H α (filled circles) and HI (empty circles) rotation curves projected onto the HI position-velocity diagram along the major axis. The contours are $n \times \sigma$, with $n=2,4,6,\dots$

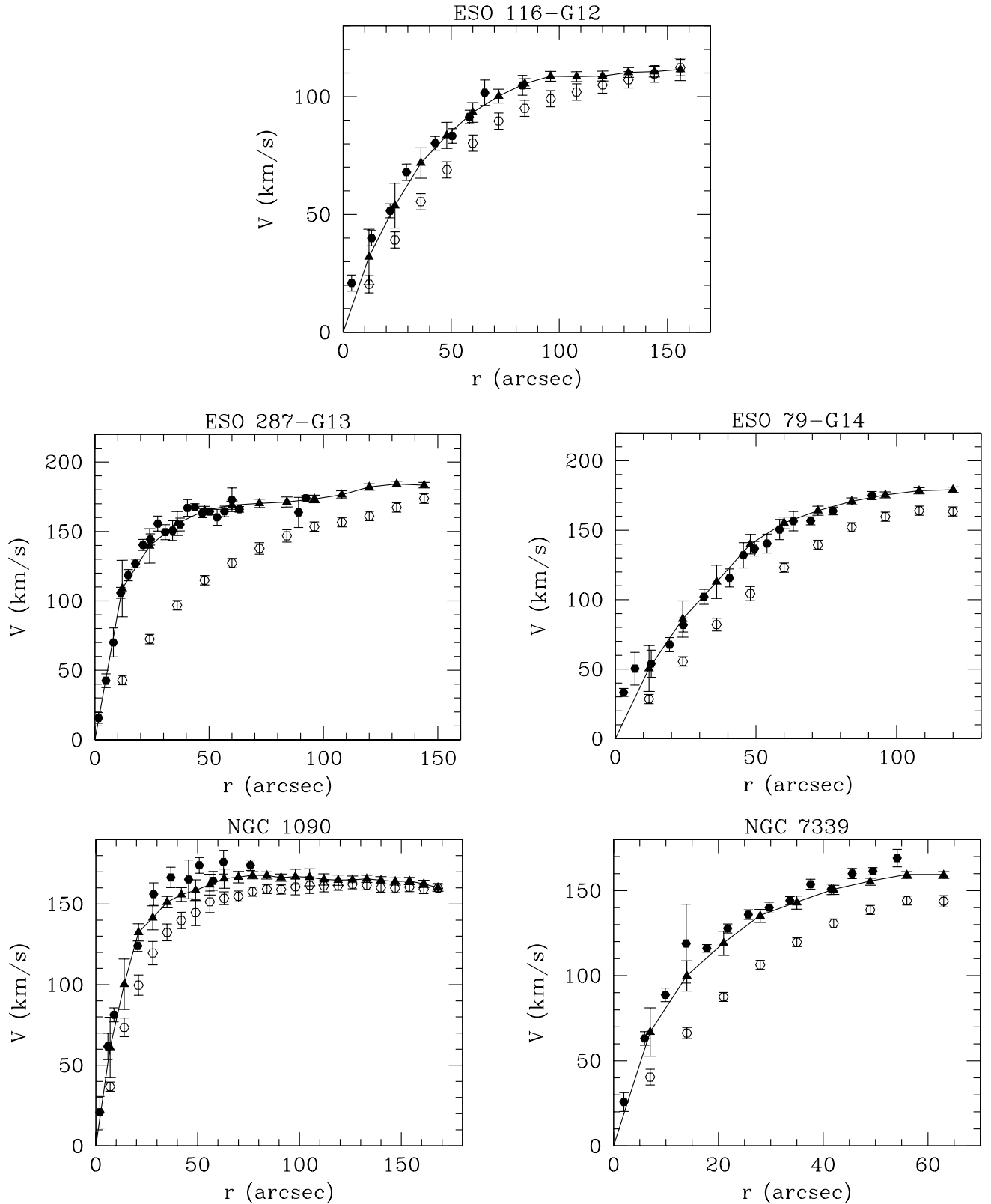


Figure 8. The rotation curves: the H α (filled circles) rotation curves, the HI corrected MET/WAMET rotation curves (filled triangles) and the HI first-moment analysis rotation curves (empty circles). The line connects the points of the corrected MET/WAMET rotation curves.

fore nearly all the mass models fitted would be consistent with the data, disabling us from putting any constraints on the dark matter distribution. The actual uncertainties on the rotation velocities are probably smaller, due to the precision than can be reached with the data cube modelling; however, they are difficult to estimate and rather subjective, therefore we keep the above estimated errors.

8 MASS MODELS

The sample allows us to test in detail different mass models with various distributions and relative amounts of dark matter.

8.1 Luminous matter

In order to study the properties of luminous and dark matter in these galaxies, we model the circular velocity $V(r)$ in terms of the disc, gas and halo components:

$$V^2(r) = V_{disc}^2(r) + V_{gas}^2(r) + V_{halo}^2(r). \quad (6)$$

$V_{disc}(r)$ is the contribution of the stellar disc, which is scaled according to the chosen (stellar, I-band) M/L ratio (hereafter Υ_*^I). In this way, the molecular gas is automatically taken into account, since it is reasonable to assume that it is distributed like the stellar component (e.g. Corbelli & Salucci 2000). The available photometry shows that the luminous matter in these galaxies is distributed like in an exponential thin disc, whose value is given in Table 1 (Mathewson, Ford & Buchhorn 1992). The exception to this is ESO 79-G14, whose profile is significantly different from exponential: for this galaxy the actual surface brightness profile was used. Υ_*^I (assumed to be constant with radius) is a free parameter in each model, however, with the condition of being larger than 0.2.

$V_{gas}(r)$ is the contribution of the gaseous disc, derived from the HI surface density distribution, scaled up by a factor 1.33 to account for primordial helium; the uncertainty of the galaxy distance is irrelevant for the present study since at no radius the HI contribution dominates the kinematics.

$V_{halo}(r)$ is the contribution of the dark matter halo, derived under a number of assumptions as discussed below.

8.2 Dark matter

8.2.1 Burkert halo

Burkert (1995) proposed an empirical density distribution of dark matter:

$$\rho_B(r) = \frac{\rho_0 r_{core}^3}{(r + r_{core})(r^2 + r_{core}^2)}. \quad (7)$$

Here, ρ_0 is the central density and r_{core} the core radius. This halo has a constant density core, $\rho_B(r) \rightarrow \rho_0$ for $r \rightarrow 0$, and a decrease of the density as r^{-3} for $r \rightarrow \infty$.

The halo has two free parameters: the core radius $a = r_{core}/r_{opt}$ (i.e., in units of the optical radius, $r_{opt} = 3.2r_d$) and the central density ρ_0 .

Other cored distributions were investigated (the pseudo-isothermal halo, van Albada et al. 1985, and the Universal Rotation Curve halo, Persic, Salucci & Stel 1996,

hereafter PSS), but they yield results which are almost indistinguishable from the Burkert halo. We include them in Table 4 for completeness.

8.2.2 Navarro, Frenk and White (NFW) halo

Navarro et al. (1996) fitted the outcome of N-body CDM simulations with a density distribution given by:

$$\rho_{NFW}(r) = \frac{\rho_s}{(r/r_s)(1 + r/r_s)^2}. \quad (8)$$

Here, ρ_s and r_s are the characteristic density and the scale radius of the distribution. They are in principle independent, but recent results (Bullock et al. 2001, Wechsler et al. 2002) show a correlation between these parameters. The NFW density distribution is then a one-parameter family, namely the virial mass M_{vir} . From Wechsler et al. (2002) we take the relations linking M_{vir} to the concentration parameter $c (= r_{vir}/r_s)$, r_s and ρ_s , at redshift $z = 0$ and for a Universe with $\Lambda = 0.7$ and $\Omega_0 = 0.3$, starting with $M_{vir} \equiv \frac{4}{3}\pi\Delta_{vir}\rho_c r_{vir}^3$ (where Δ_{vir} is the virial overdensity and its value is about 337 at $z = 0$, ρ_c is the critical density of the Universe and r_{vir} is the virial radius):

$$c \simeq 20 \left(\frac{M_{vir}}{10^{11} M_\odot} \right)^{-0.13}, \quad r_s \simeq 5.7 \left(\frac{M_{vir}}{10^{11} M_\odot} \right)^{0.46} \text{ kpc} \quad (9)$$

$$\rho_s \simeq \frac{101}{3} \frac{c^3}{\ln(1+c) - \frac{c}{1+c}} \rho_c. \quad (10)$$

NFW halo has then a central density cusp, with $\rho_{NFW} \propto r^{-1}$ for $r \rightarrow 0$, and a profile/amplitude which is controlled by a free parameter M_{vir} .

Notice that in principle, adiabatic contraction of the primordial dark matter halo due to baryon infall should be taken into account, but since the effect is to render the halo even more concentrated, aggravating thus the known problems of the NFW haloes, we neglect it.

We constrain the virial halo mass to be $M_{vir} < 8 \times 10^{11} M_\odot$, in that, for a low luminosity spiral, it must presumably be substantially lower than that of the Milky Way and other very luminous galaxies, for which it is safely estimated: $M_{vir} \simeq 2 \times 10^{12} M_\odot$ (Chengalur, Salpeter & Terzian 1993, Wilkinson & Evans 1999). This constraint affects only N7339 and ESO 79-G14, due to the relatively limited extension of their HI rotation curves, which prevents to rule out large Λ CDM haloes.

8.2.3 Moore halo

Recent numerical simulations by Moore et al. (1998) yielded a more concentrated density profile:

$$\rho_{Moore}(r) = \frac{\rho_s}{(r/r_s)^{1.5}(1 + (r/r_s)^{1.5})}, \quad (11)$$

where ρ_s and r_s are the characteristic density and the scale radius of the distribution. This density distribution has an even steeper cusp ($\rho_{Moore} \propto r^{-1.5}$ for $r \rightarrow 0$) than the previous one. Similarly to the NFW halo, we consider this profile as having only one free parameter. Following Moore et al. (1999), we define c_{Moore} as being 1.8 times smaller than c_{NFW} ; it is then derived from Eq. 9. For a given virial radius, the scale radius r_s of the Moore halo will

then be 1.8 times larger than its corresponding quantity for the NFW halo. ρ_s can be derived from:

$$\rho_s = \frac{101}{2} \frac{c^3}{\ln(1+c^{1.5})} \rho_c. \quad (12)$$

Also in this case we constrain the virial halo mass to be lower than $8 \times 10^{11} M_\odot$.

8.2.4 HI scaling

Early studies of HI rotation curves (Bosma 1981) noted the fact that the ratio between the HI surface density and the dark matter surface density is approximately constant in the outer parts of galaxies (but see Corbelli & Salucci 2000). This led to the hypothesis that dark matter could in some way be associated with the HI disc and distributed in the same manner; this is what is reasonable to expect in the case of models considering for instance H_2 clumps as a component of dark matter (Pfenniger, Combes & Martinet 1994). In this case the scaling factor for the HI contribution to the rotation curve is a free parameter.

8.3 MOND

According to MOND, the law of Modified Newtonian Dynamics (Milgrom 1983), there exists a certain acceleration a_0 below which Newton's law of gravity is no longer valid and the expression for the gravitational acceleration reads:

$$g(r) = [GM(r)a_0]^{1/2}/r, \quad (13)$$

where $M(r)$ account for the stellar and gaseous components and $a_0 = 1.2 \times 10^{-8} \text{ cm s}^{-2}$ (Begeman, Broeils & Sanders 1991).

9 MASS MODELLING RESULTS

The fits were performed by a χ^2 -minimisation, considering both the rotational velocities and their logarithmic gradients ($\nabla = \frac{d \log V(r)}{d \log r}$), which bear a crucial information on the matter distribution in a galaxy (see Persic & Salucci 1990). The total χ^2 value to be minimised then is $\chi_{tot}^2 = \chi_{vel}^2 + \chi_{\nabla}^2$. It is worthwhile to point out that the χ^2 values should only be considered as a way to compare the different fits within the same galaxy, rather than a probability indicator, because the choice of the error bars is quite subjective and we plot two points per beam, so the points are not independent; the goodness of a particular mass model is also related to the fraction of observational points that it hits within 1σ as well as the ones that it badly misses.

In Figs. 9 to 13 we show, for each galaxy, the results of the fits, the residuals ($V_{obs} - V_{model}$) of the fits and the 1σ probability contours in parameter space. The case of NGC 7339 will be discussed in Appendix A.

The Burkert profile – so as any cored profile – has the best fits to the rotation curves, with no systematic deviation from the observed rotation curves seen in all galaxies. None of our ~ 100 data points (considering the five galaxies together) is inconsistent with this model, having a residual larger than 3σ (where σ is the observational error). The stellar I-band mass-to-light ratios, which lie between 0.5 and 1.8, are consistent with population synthesis models (e.g.,

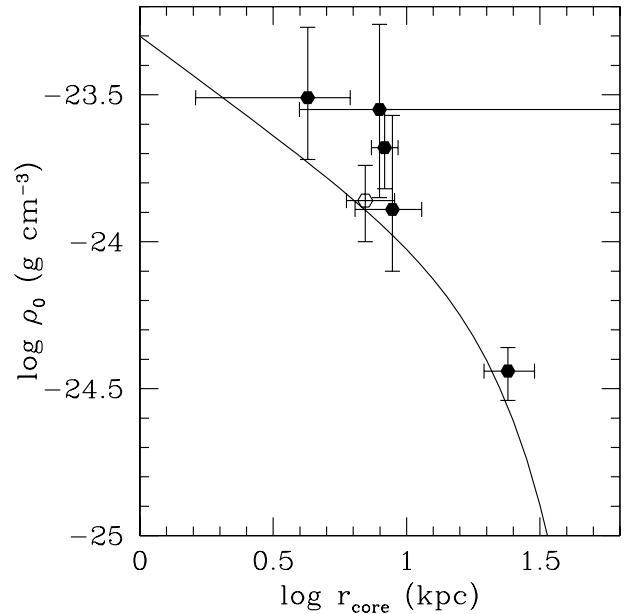


Figure 14. Relation between the Burkert central density and Burkert core radius; the solid line is the relation found by Burkert (1995) and extended to spiral galaxies by Salucci & Burkert (2000): $\rho_0 = 5 \times 10^{-24} r_{core}^{-2/3} e^{-(r_{core}/27)^2} \text{ g cm}^{-3}$. The open circle represents DDO 47 (Salucci et al. 2003) and the filled circles are the galaxies of the present sample.

Bell & de Jong 2001). The core radii are in the range $(0.7 - 2.3) \times r_{opt}$, and the central densities are between $(0.4 - 3) \times 10^{-24} \text{ g cm}^{-3}$. In Fig. 14 we plot the galaxies of our sample in the $\rho_0 - r_{core}$ plane of Burkert (1995), slightly adapted to spiral galaxies by Salucci & Burkert (2000): despite a certain scatter, they roughly follow the relation, which certainly has an implication for the nature of dark matter.

The minimum χ^2 values for the NFW haloes are significantly higher than for the Burkert haloes. The former fail to reproduce both the velocities and the shape of the observed rotation curves. Moreover, there is a systematic effect in the predicted velocities, in the sense that the NFW haloes predict velocities in the central parts that are too high. A significant number of data points (9) is totally inconsistent (i.e., residuals larger than 3σ) with the fits performed with the NFW halo; if we consider the points with residuals larger than 2σ their number increases to 22. An additional problem of the NFW haloes is that the emerging Υ_*^I are generally small and in one case unacceptably low; in this case the extreme lower limit of 0.2 is reached. We also attempted to reproduce the data by leaving c as a free parameter, instead of using Eq. 9: no appreciable improvement of the fits is found. Moreover, the values of c and M_{vir} are in some cases completely unrealistic, in particular we obtain very low values of c .

The Moore haloes provide even worse results, with very high χ^2 values compared to the cored haloes, and velocities that are far too high in the inner parts, which are a consequence of the predicted steep central cusps. The inability of the Moore haloes to reproduce the observed kinematics appears also in the large number of points (25) having residuals larger than 3σ . Notice that recent simulations

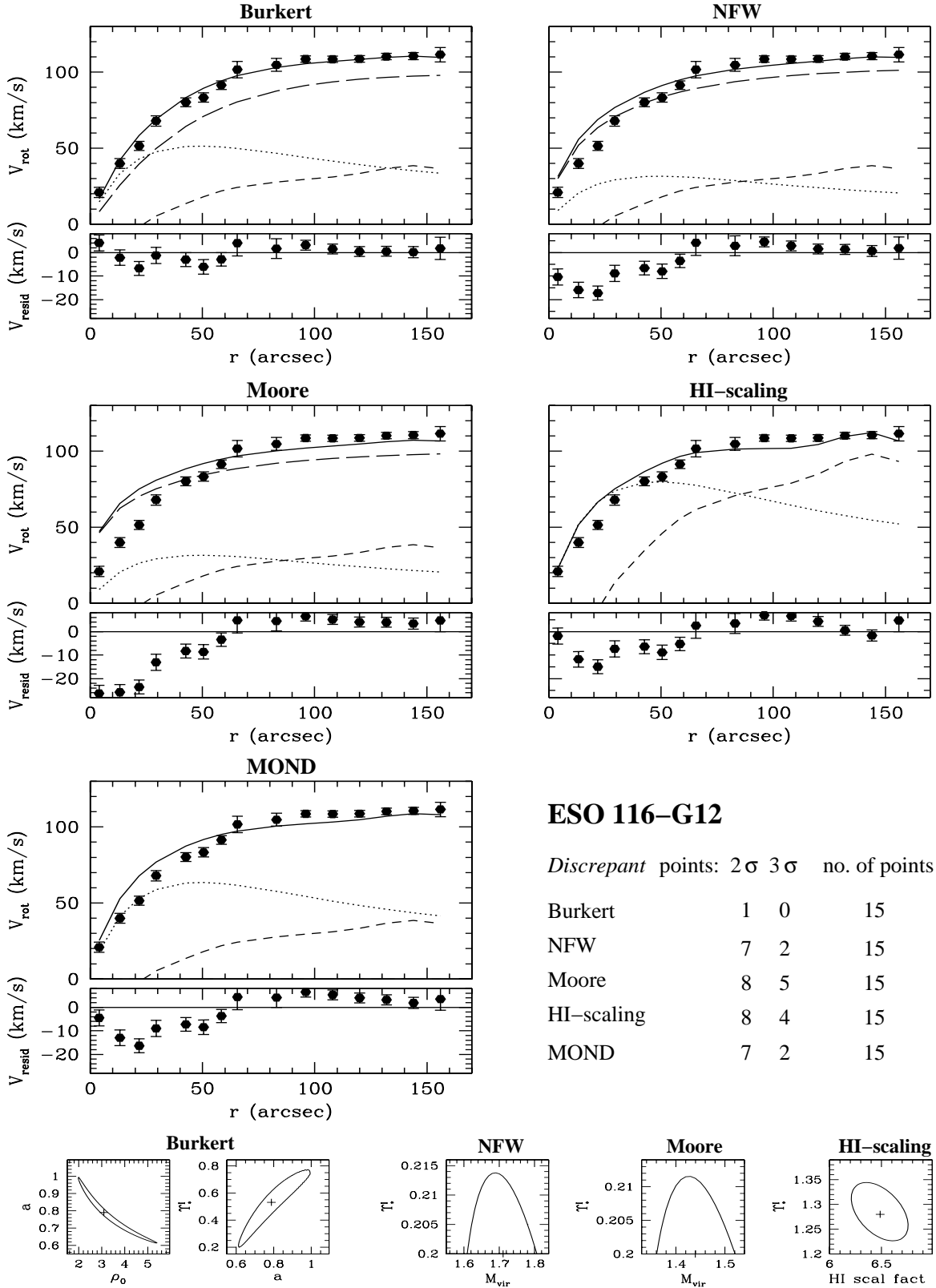


Figure 9. Mass models for the galaxy ESO 116-G12. The solid line represents the best-fitting model, the long-dashed line is the contribution of the dark matter halo, and the dotted and short-dashed lines are the contributions of the stellar and gaseous discs, respectively. 1 kpc corresponds to 13''. Below the rotation curves we show the residuals ($V_{obs} - V_{model}$). At the bottom we plot the 1 σ probability contours in the parameter space, where the crosses indicate the best-fitting values, ρ_0 is in units of $10^{-24} \text{ g cm}^{-3}$ and M_{vir} is in units of $10^{11} M_{\odot}$. We also give the number of discrepant points, with residuals is larger than 2 σ and 3 σ , where σ is the observational error on $V_{obs}(r)$ at radius r .

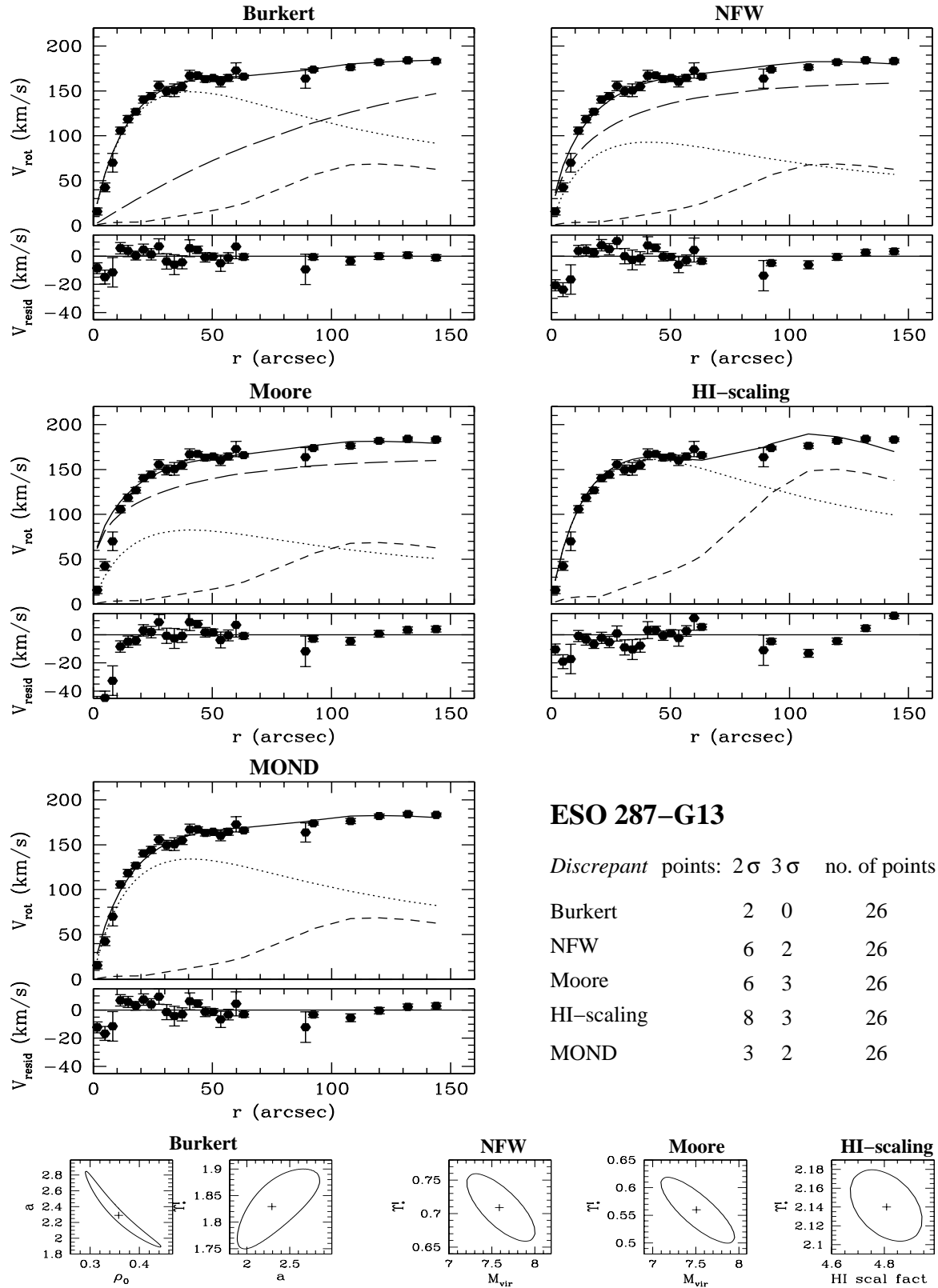


Figure 10. Mass models for the galaxy ESO 287-G13 (see Fig. 9 for an explanation of layout and symbols). 1 kpc corresponds to $5''/8$.

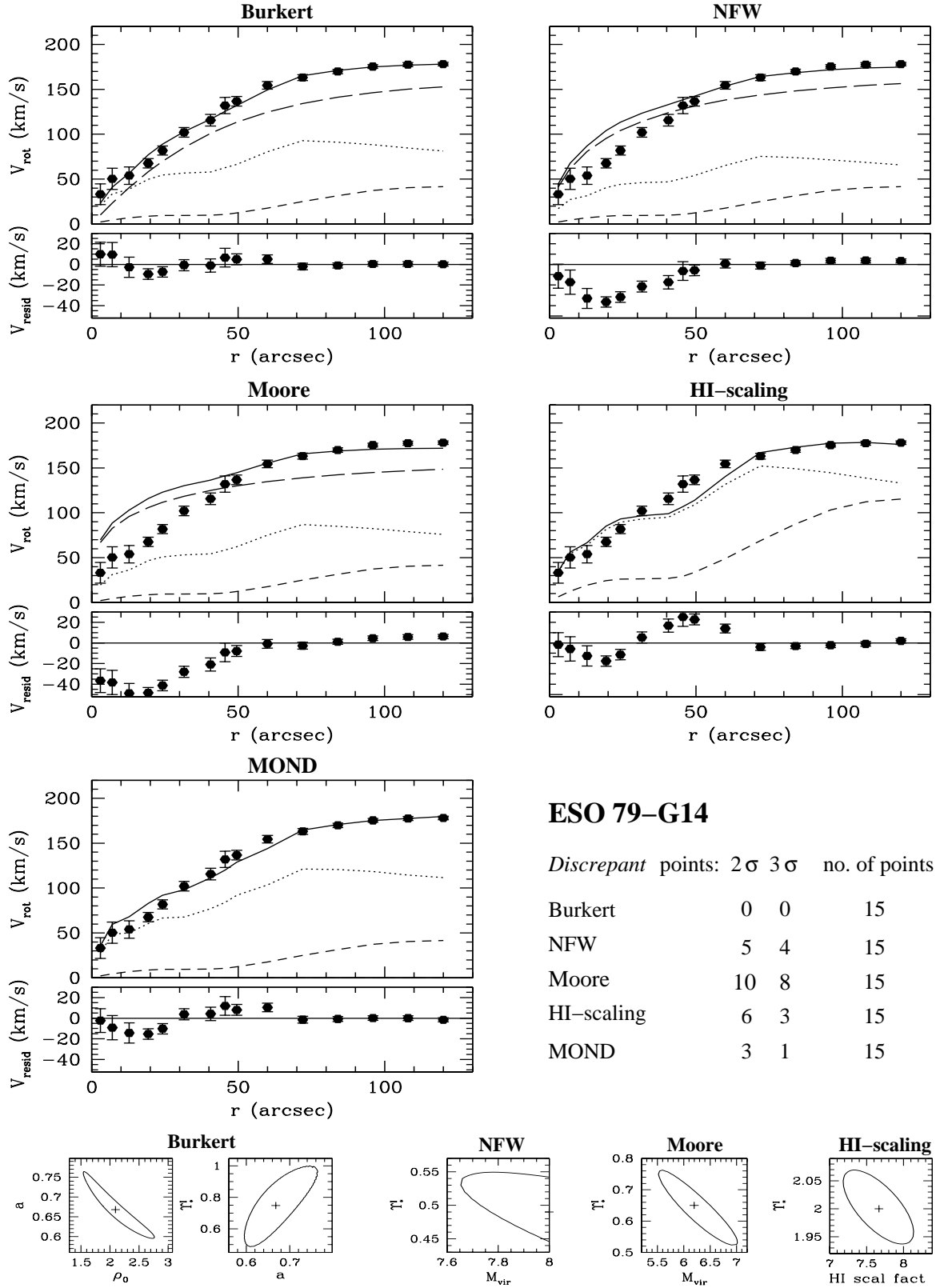


Figure 11. Mass models for the galaxy ESO 79-G14 (see Fig. 9 for an explanation of layout and symbols). 1 kpc corresponds to $6''$.

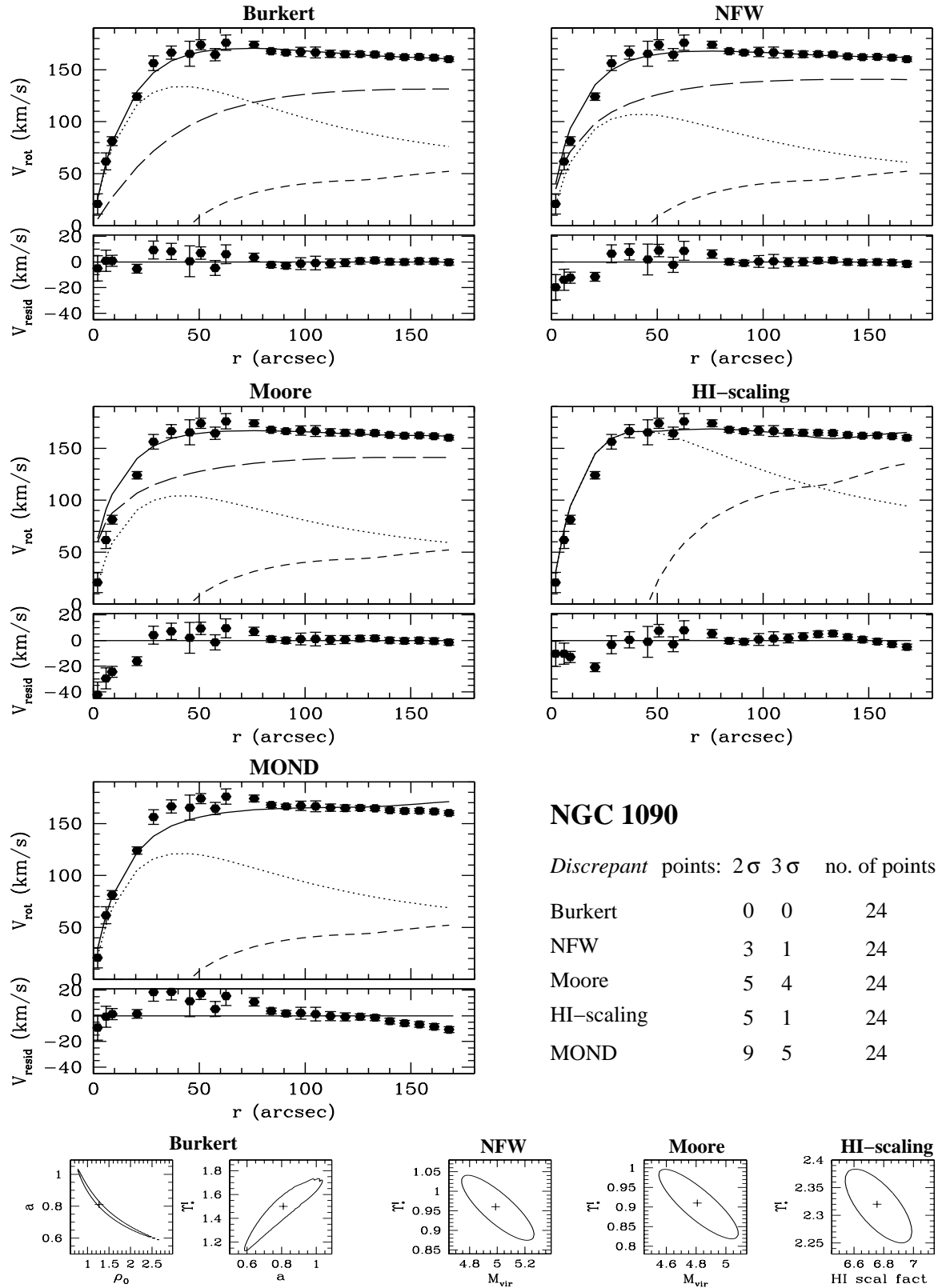


Figure 12. Mass models for the galaxy NGC 1090 (see Fig. 9 for an explanation of layout and symbols). 1 kpc corresponds to $5''7$.

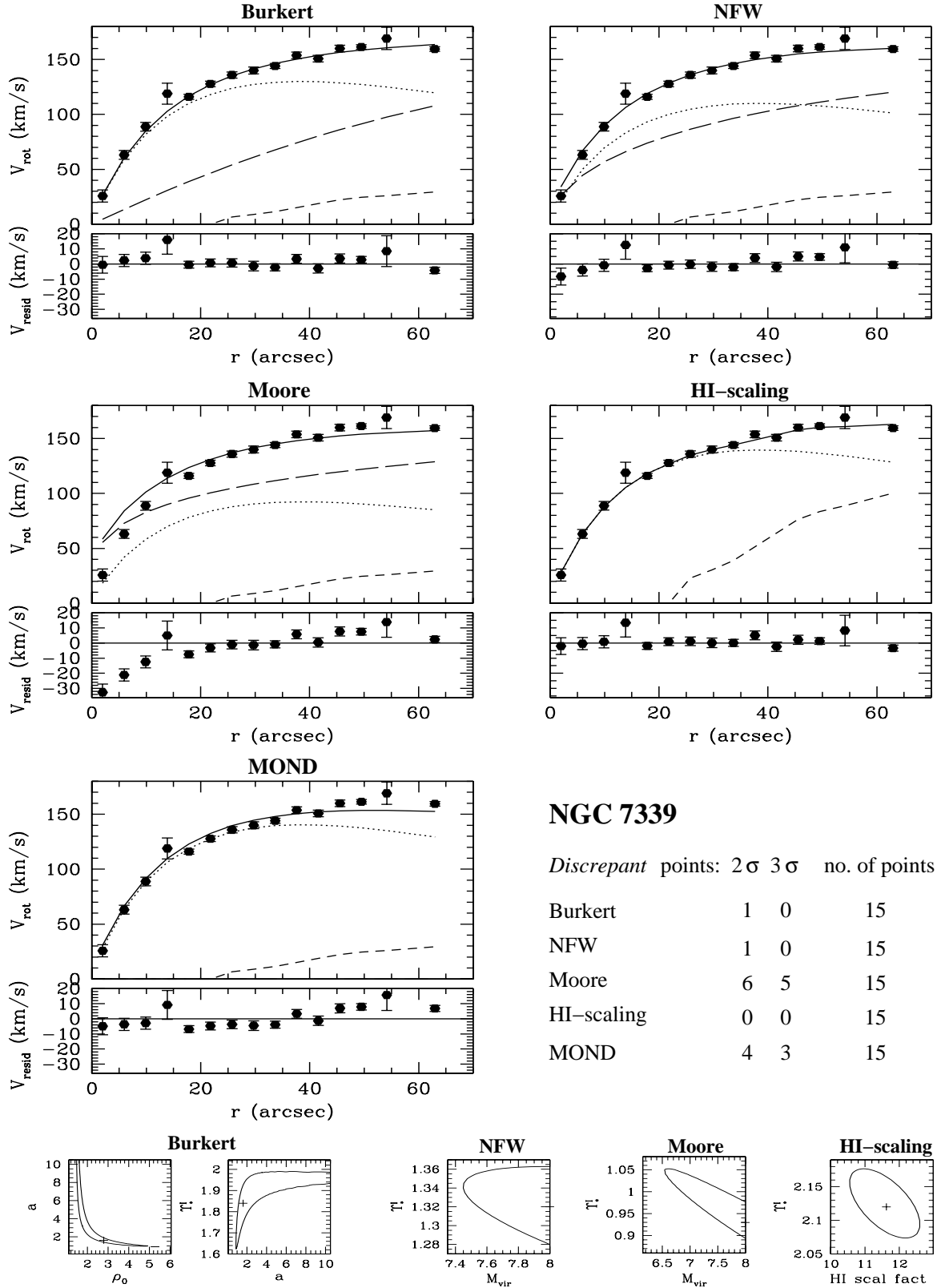


Figure 13. Mass models for the galaxy NGC 7339 (see Fig. 9 for an explanation of layout and symbols). 1 kpc corresponds to $11''6$.

Table 4. Best-fitting results: parameters and associated errors, reduced χ^2 . $a = r_{core}/r_{opt}$, ρ_0 is in units of 10^{-24} g cm $^{-3}$ and M_{vir} is in units of 10^{11} M $_{\odot}$.

Halo type	Parameter	ESO 116-G12	ESO 287-G13	ESO 79-G14	NGC 1090	NGC 7339
Burkert	a	$0.79^{+0.21}_{-0.18}$	$2.29^{+0.56}_{-0.41}$	$0.67^{+0.08}_{-0.07}$	$0.81^{+0.23}_{-0.22}$	$1.60^{+\infty}_{-0.79}$
	ρ_0	$3.1^{+2.3}_{-1.2}$	$0.36^{+0.08}_{-0.07}$	$2.2^{+0.6}_{-0.7}$	$1.3^{+1.4}_{-0.5}$	$2.8^{+2.7}_{-1.4}$
	Υ_*^I	$0.53^{+0.24}_{-0.33}$	$1.83^{+0.07}_{-0.08}$	$0.73^{+0.27}_{-0.25}$	$1.50^{+0.24}_{-0.36}$	$1.84^{+0.15}_{-0.24}$
	χ_{red}^2	3.0	1.2	1.1	0.4	1.2
URC	a	$0.59^{+0.19}_{-0.12}$	$2.20^{+0.42}_{-0.36}$	$0.67^{+0.09}_{-0.08}$	$0.56^{+0.31}_{-0.16}$	$1.47^{+3.94}_{-0.55}$
	ρ_0	$4.2^{+2.7}_{-1.9}$	$0.28^{+0.06}_{-0.04}$	$1.5^{+0.4}_{-0.3}$	$1.9^{+2.0}_{-1.1}$	$2.3^{+1.5}_{-0.8}$
	Υ_*^I	$0.30^{+0.30}_{-0.10}$	$1.86^{+0.06}_{-0.09}$	$0.90^{+0.20}_{-0.24}$	$1.32^{+0.33}_{-0.28}$	$1.85^{+0.14}_{-0.17}$
	χ_{red}^2	2.5	1.2	0.9	0.4	1.1
pseudo-isothermal	a	$0.40^{+0.10}_{-0.12}$	$1.50^{+0.29}_{-0.32}$	$0.42^{+0.09}_{-0.05}$	$0.37^{+0.15}_{-0.13}$	$1.10^{+3.61}_{-0.38}$
	ρ_0	$3.6^{+2.3}_{-1.3}$	$0.30^{+0.08}_{-0.05}$	$1.6^{+0.5}_{-0.5}$	$1.7^{+2.1}_{-1.0}$	$2.3^{+1.5}_{-0.9}$
	Υ_*^I	$0.50^{+0.21}_{-0.24}$	$1.84^{+0.07}_{-0.09}$	$0.96^{+0.24}_{-0.17}$	$1.50^{+0.22}_{-0.26}$	$1.85^{+0.15}_{-0.17}$
	χ_{red}^2	2.8	1.2	1.3	0.5	1.1
NFW	M_{vir}	$1.71^{+0.10}_{-0.12}$	$7.59^{+0.42}_{-0.38}$	$8.00^{+0.00}_{-0.35}$	$4.99^{+0.27}_{-0.26}$	$8.00^{+0.00}_{-0.56}$
	Υ_*^I	$0.20^{+0.01}_{-0.00}$	$0.71^{+0.05}_{-0.05}$	$0.49^{+0.06}_{-0.04}$	$0.96^{+0.08}_{-0.09}$	$1.32^{+0.04}_{-0.04}$
	χ_{red}^2	5.2	2.7	7.2	1.1	1.4
Moore	M_{vir}	$1.44^{+0.10}_{-0.12}$	$7.51^{+0.34}_{-0.41}$	$6.20^{+0.81}_{-0.69}$	$4.81^{+0.27}_{-0.25}$	$8.00^{+0.00}_{-1.47}$
	Υ_*^I	$0.20^{+0.01}_{-0.00}$	$0.56^{+0.06}_{-0.06}$	$0.65^{+0.11}_{-0.13}$	$0.91^{+0.09}_{-0.08}$	$0.93^{+0.12}_{-0.04}$
	χ_{red}^2	10.6	6.6	13.0	2.7	5.3
Hi-scal	scal fact	$6.49^{+0.28}_{-0.28}$	$4.81^{+0.13}_{-0.14}$	$7.67^{+0.45}_{-0.49}$	$6.76^{+0.23}_{-0.23}$	$11.63^{+0.97}_{-1.08}$
	Υ_*^I	$1.28^{+0.06}_{-0.05}$	$2.14^{+0.04}_{-0.04}$	$2.00^{+0.07}_{-0.06}$	$2.32^{+0.07}_{-0.07}$	$2.12^{+0.06}_{-0.05}$
	χ_{red}^2	18.8	11.1	7.0	2.8	1.1
MOND	Υ_*^I	$0.81^{+0.02}_{-0.03}$	$1.48^{+0.02}_{-0.02}$	$1.24^{+0.02}_{-0.02}$	$1.23^{+0.02}_{-0.02}$	$2.15^{+0.03}_{-0.03}$
	χ_{red}^2	5.2	1.9	2.5	3.4	3.6

(Navarro et al. 2003) predict, at the innermost resolved radius, a slope of 1.2 (approximately intermediate between the NFW and the Moore profile) in the radial density profile of a typical galaxy and that they rule out the Moore profile.

The HI-scaling and the MOND models give reasonable results in a few cases, but with some decisive counter-examples: we have a significant number of points that are inconsistent with the fits in both cases. In particular, the present data have a resolution such that MOND is not able to fit them. The values of the HI scaling factors are consistent with previous studies (Hoekstra et al. 2001). Leaving the MOND acceleration parameter a_0 as a free parameter only slightly improves the quality of the fits: they are always significantly worse than in case of the cored haloes. The same holds if we leave a reasonable (25%) uncertainty on the adopted distance.

10 CONCLUSIONS

We have presented an analysis of HI data cubes of a sample of five low-luminosity spiral galaxies that are used to derive the distribution of dark matter within these galaxies, along with available H α and I-band photometric data.

We found a new method (the MET/WAMET method) for deriving the HI rotation curves, which was needed to take into account a) a position angle that varies with radius (this is needed as the tilted-ring modelling of the velocity field could be used in only one case), and b) the asymmetry of the velocity profiles, because the galaxies of our sample have a high inclination, and projection effects yield asymmetric velocity profiles. Corrections were applied in order to account for any effects that artificially broaden the HI profiles.

The rotation curves derived in this way passed a crucial test, i.e. the construction of model data cubes using these rotation curves as an input. In some cases the HI rotation

curves derived from MET/WAMET required a small modification, mostly in the inner parts. After these small corrections the model data cubes are in very good agreement with the observations, contrary to model data cubes constructed using rotation curves derived from other “classical” methods. Our final HI rotation curves are consistent with the H α data, but up to three times more extended.

In galaxies well suited for inferring the distribution of dark matter, we were able to trace the total potential via the rotation velocity and to derive the density distribution of dark matter.

From the analysis of combined H α and HI rotation curves we reach the following conclusions:

- Cored haloes uniquely fit the rotation curves, with core radii of order r_{opt} and central densities of order 10^{-24} g cm $^{-3}$.
- NFW haloes cannot represent the dark matter haloes around the galaxies of our sample: they fit badly and a significant number of data points is inconsistent with the fits.
- The situation is even worse for the Moore model, as implied by its steeper inner profile.
- There are cases in which for radii in the range $(1 - 4)r_d$ the Burkert and NFW halo rotation curves are similar; this may explain why in the literature cases can be found (e.g. Jimenez, Verde & Oh 2003) in which both models fit equally well a rotation curve of small extension and limited resolution.

We thus reach the conclusion that the galaxies of the present sample are uniquely successfully fitted by cored haloes, with a core size comparable to the optical radius. This suggests the existence of a well-defined scale length in dark matter haloes, linked to the luminous matter, which is totally unexpected in the framework of CDM theory (see Salucci & Burkert 2000).

ACKNOWLEDGEMENTS

The authors wish to thank the referee, Albert Bosma, for his comments that improved the outline and the quality of the paper. We thank Thomas Fritz and Christian Brüns for help with the observations. GG and DV are grateful for financial support from the *Deutsche Forschungsgemeinschaft* under number GRK 118 “The Magellanic System, Galaxy Interaction and the Evolution of Dwarf Galaxies”. UK is very grateful to the kind hospitality as SISSA during several visits.

REFERENCES

- Begeman, K. G., 1989, A&A, 223, 47
 Begeman, K. G., Broeils, A. H., Sanders, R. H., 1991, MNRAS, 249, 523
 Bell, E. F., de Jong, R. S., 2001, ApJ, 550, 212
 Borriello, A., Salucci, P., 2001, MNRAS, 323, 285
 Bosma, A., 1981, AJ, 86, 1825
 Braun, R., 1997, ApJ, 484, 637
 Briggs, D., 1995, Ph.D. thesis, New Mexico Inst. Mining and Technology
 Bullock, J.S., Kolatt, T.S., Rachel, Y.S., Somerville, S., Kravtsov, A.V., Klypin, A.A., Primack, J.R., Dekel, A., 2001, MNRAS, 321, 559
 Burkert, A., 1995, ApJ, 447, L25
 Burkert, A., Silk, J., 1997, ApJ, 488, L55
 Chengalur, J. N., Salpeter, E. E., Terzian, Y., 1993, ApJ, 419, 30
 Corbelli, E., Salucci, P., 2000, MNRAS, 311, 441
 de Blok, W. J. G., McGaugh, S. S., Rubin, V. C., 2001, AJ, 122, 2396
 de Blok, W. J. G., Bosma, A., 2002, A&A, 385, 816
 de Blok, W. J. G., Bosma, A., McGaugh, S., 2003, MNRAS, 340, 657
 Flores, R., Primack, J.R., 1994, ApJ, 427, L1
 Fraternali, F., Oosterloo, T., Sancisi, R., van Moorsel, G., 2002, ApJ, 562, L47
 Garcia-Ruiz, I., Sancisi, R., Kuijken, K., 2002, A&A, 394, 769
 Gentile, G., Fraternali, F., Klein, U., Salucci, P., 2003, A&A, 405, 969
 Hoekstra, H., van Albada, T. S., Sancisi, R., 2001, MNRAS, 323, 453
 Jimenez, R., Verde, L., Oh, S. P., 2003, MNRAS, 339, 243
 Kamphuis, J., 1993, Ph.D. thesis, Univ. Groningen
 Kravtsov, A.V., Klypin, A.A., Bullock, J.S., Primack, J.R., 1998, ApJ, 502, 48
 Mathewson, D. S., Ford, V. L., Buchhorn, M., 1992, ApJS, 81, 413
 McGaugh, S.S., de Blok, W.J.G., 1998, ApJ, 449, 41
 Milgrom, M., 1983, ApJ, 270, 365
 Moore, B., 1994, Nat., 370, 629
 Moore, B., Governato, F., Quinn, T., Stadel, J., Lake, G., 1998, ApJ, 499, L5
 Moore, B., Quinn, T., Governato, F., Stadel, J., Lake, G., 1999, MNRAS, 310, 1147
 Navarro, J.F., Frenk, C.S., White, S.D.M., 1996, ApJ, 462, 563
 Navarro, J. F., Hayashi, E., Power, C., Jenkins, A., Frenk, C. S., White, S. D. M., Springel, V., Stadel, J., Quinn, T. R., 2003, MNRAS in press, astro-ph/0311231
 Persic, M., Salucci, P., 1988, MNRAS, 234, 131
 Persic, M., Salucci, P., 1990, MNRAS, 245, 577
 Persic, M., Salucci, P., 1995, ApJS, 99, 501
 Persic, M., Salucci, P., Stel, F., 1996, MNRAS, 281, 27P
 Pfenniger, D., Combes, F., Martinet, L., 1994, A&A, 285, 79
 Primack, J.R. 2002, preprint, astro-ph/0205391
 Rhee, G., Klypin, A., Valenzuela, O., 2003, ASP Conference Series, in press, preprint (astro-ph/0311020)
 Rubin, V.C., Thonnard, N., Ford, W.K.Jr., 1980, ApJ, 238, 471
 Salucci, P., 2001, MNRAS 320, L1
 Salucci, P., Burkert, A., 2000, ApJ, 537, L9
 Salucci, P., Walter, F.M., Borriello, A., 2003, A&A, 409, 53
 Sancisi, R., Allen, R. J., 1979, A&A, 74, 73
 Sault R. J., Teuben P. J., Wright M. C. H., 1995, in Shaw R., Payne H. E., Hayes J. J. E., eds, ASP Conf. Ser. Vol. 77, Astronomical Data Analysis Software and Systems IV. Astron. Soc. Pac., San Francisco, p. 433
 Simon, J. D., Bolatto, A. D., Leroy, A., Blitz, L., 2003, ApJ, 596, 957

- Sofue, Y., Tutui, Y., Honma, M., Tomita, A., 1997, *AJ*, 115, 2428
- Swaters, R. A., Sancisi, R., van der Hulst, J. M., 1997, *ApJ*, 491, 140
- Swaters, R. A., Madore, B. F., van den Bosch, F. C., Balcells, M., 2003, *ApJ*, 583, 732
- Swaters, R.A., Verheijen, M. A. W., Bershadsky, M. A., Andersen, D. R., 2003, *ASP Conference Series*, in press, preprint (astro-ph/0311480)
- van Albada, T.S., Bahcall, J.N., Begeman, K., Sancisi, R., 1985, *ApJ*, 295, 305
- van den Bosch, F.C., Robertson, B.E., Dalcanton, J., de Blok, W.J.G., 2000, *AJ*, 119, 1579
- van den Bosch, F. C., Swaters, R. A., 2001, *MNRAS*, 325, 1017
- van der Hulst, J. M., Terlouw, J. P., Begeman, K. G., Zwitser, W., Roelfsema, P. R., 1992, *ASP Conf. Ser.* 25, Worrall D.M., Biemesderfer, C., & Barnes, J., eds., p. 131
- Vergani, D., Gentile, G., Dettmar, R.-J., Klein, U., 2004, *A&A* submitted
- Verheijen, M. A. W., Sancisi, R., 2001, *A&A*, 370, 765
- Warmels, R. H., 1988, *A&AS*, 72, 427
- Wechsler, R. H., Bullock, J. S., Primack, J. R., Kravtsov, A. V., Dekel, A., 2002, *ApJ*, 568, 52
- Weldrake, D.T.F., de Blok, W. J. G., Walter, F., 2003, *MNRAS*, 340, 12
- Wilkinson, M. I., Evans, N. W., 1999, *MNRAS*, 310, 645

APPENDIX A: THE CASE OF NGC 7339

The galaxy NGC 7339, due to the small extent of the kinematical data and the value of its dark mass, shows a degeneracy between the predicted Burkert and NFW halo rotation curves. As can be seen in Fig. 13 and in Table 4, both models provide equally good fits to the rotation curve. This is not due to the fitting procedure but it derives from the fact that both models have similar predictions. We treat in detail this case to show that Λ CDM haloes, for certain virial masses and in certain ranges of radii has a radial profile that meets that of the Universal Rotation Curve (see PSS).

First, let us notice that from Table 1 that the rotation curve of this galaxy has a small spatial extent, i.e. about 5 kpc. Then in Fig. A1 (left panel) we show the NFW halo rotation curve, very different in general from the derived actual haloes (Salucci & Burkert 2000), for objects having a number of virial masses, ranging from $1 \times 10^{11} M_{\odot}$ to $3 \times 10^{12} M_{\odot}$. However, as shown in the right panel of Fig. A1, for virial masses close to about $1 \times 10^{12} M_{\odot}$, and for radii up to 5 kpc, the NFW and Burkert halo rotation curves almost coincide; this similarity, combined with the uncertainty on Υ_{*}^I , is the reason for the equal quality of the two fits.

With the data used here we cannot probe the regions of NGC 7339 where the difference is noticeable. Therefore, for galaxies having $V(r_{opt})$ approximately in the range 120–170 km s^{-1} and for the radial range $1 < r/r_d < 4$, in order to distinguish between the two cases, we need kinematical information at larger radii. At smaller and larger $V(r_{opt})$ the two profiles are intrinsically much more different and the comparison is easier (see PSS).

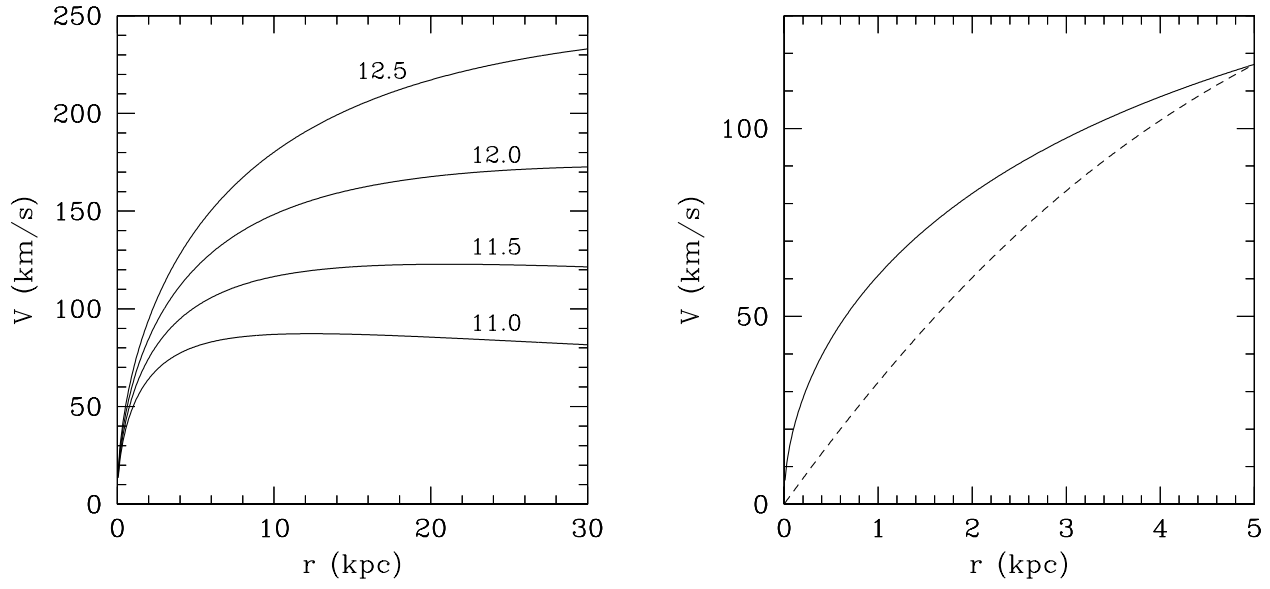


Figure A1. Left: NFW halo rotation curves for galactic haloes; the values of $\log(M_{vir}/M_{\odot})$ are indicated on the plot. Notice the very large differences with respect to the Universal Rotation Curve (Fig. 6 of PSS). Right: NFW halo rotation curve (solid line) for an object with $M_{vir} = 8 \times 10^{11} M_{\odot}$ and a Burkert halo rotation curve with $r_{core} = 6$ kpc and $\rho_0 = 4.5 \times 10^{-24} \text{ g cm}^{-3}$, for radii up to 5 kpc.